



ARL-TR-8145 • SEP 2017



US Army Research Laboratory

Incorporating Variational Local Analysis and Prediction System (vLAPS) Analyses with Nudging Data Assimilation: Methodology and Initial Results

**by Brian P Reen, Yuanfu Xie, Huaqing Cai, Steve Albers,
Robert E Dumais Jr, and Hongli Jiang**

Approved for public release; distribution is unlimited.

NOTICES

Disclaimers

The findings in this report are not to be construed as an official Department of the Army position unless so designated by other authorized documents.

Citation of manufacturer's or trade names does not constitute an official endorsement or approval of the use thereof.

Destroy this report when it is no longer needed. Do not return it to the originator.



Incorporating Variational Local Analysis and Prediction System (vLAPS) Analyses with Nudging Data Assimilation: Methodology and Initial Results

by Brian P Reen, Huaqing Cai, and Robert E Dumais Jr
Computational and Information Sciences Directorate, ARL

Yuanfu Xie
National Oceanic and Atmospheric Administration, Boulder, CO

Steve Albers and Hongli Jiang
National Oceanic and Atmospheric Administration, Boulder, CO
Cooperative Institute for Research in the Atmosphere, Colorado State University, Boulder, CO

REPORT DOCUMENTATION PAGE				Form Approved OMB No. 0704-0188	
<p>Public reporting burden for this collection of information is estimated to average 1 hour per response, including the time for reviewing instructions, searching existing data sources, gathering and maintaining the data needed, and completing and reviewing the collection information. Send comments regarding this burden estimate or any other aspect of this collection of information, including suggestions for reducing the burden, to Department of Defense, Washington Headquarters Services, Directorate for Information Operations and Reports (0704-0188), 1215 Jefferson Davis Highway, Suite 1204, Arlington, VA 22202-4302. Respondents should be aware that notwithstanding any other provision of law, no person shall be subject to any penalty for failing to comply with a collection of information if it does not display a currently valid OMB control number.</p> <p>PLEASE DO NOT RETURN YOUR FORM TO THE ABOVE ADDRESS.</p>					
1. REPORT DATE (DD-MM-YYYY) September 2017		2. REPORT TYPE Technical Report		3. DATES COVERED (From - To) July 2014–February 2017	
4. TITLE AND SUBTITLE Incorporating Variational Local Analysis and Prediction System (vLAPS) Analyses with Nudging Data Assimilation: Methodology and Initial Results				5a. CONTRACT NUMBER	
				5b. GRANT NUMBER	
				5c. PROGRAM ELEMENT NUMBER	
6. AUTHOR(S) Brian P Reen, Yuanfu Xie, Huaqing Cai, Steve Albers, Robert E Dumais Jr, and Hongli Jiang				5d. PROJECT NUMBER	
				5e. TASK NUMBER	
				5f. WORK UNIT NUMBER	
7. PERFORMING ORGANIZATION NAME(S) AND ADDRESS(ES) US Army Research Laboratory Computational and Information Sciences Directorate (ATTN: RDRL-CIE-M) 2800 Powder Mill Road, Adelphi, MD 20783-1138				8. PERFORMING ORGANIZATION REPORT NUMBER ARL-TR-8145	
9. SPONSORING/MONITORING AGENCY NAME(S) AND ADDRESS(ES)				10. SPONSOR/MONITOR'S ACRONYM(S)	
				11. SPONSOR/MONITOR'S REPORT NUMBER(S)	
12. DISTRIBUTION/AVAILABILITY STATEMENT Approved for public release; distribution is unlimited.					
13. SUPPLEMENTARY NOTES					
14. ABSTRACT <p>The potential value of combining 2 data assimilation methodologies to improve mesoscale meteorological model predictions is investigated using a case day with strong convection. The variational version of the Local Analysis and Prediction System (vLAPS) and both analysis and observation nudging data assimilation are applied both separately and together. The combination of methods is designed to combine the benefits of the gradual and persistent application of the effects of observations during a pre-forecast gained from nudging with the ability to assimilate a wide variety of observation types gained from vLAPS. Multiple cycles of 1-km horizontal grid spacing forecasts of the Advanced Research version of the Weather Research and Forecasting model were completed for 20 May 2013 over the southern Great Plains. The results suggest potential value in this combination data assimilation system, but further analysis of this case is required as well as application of the technique to additional case days.</p>					
15. SUBJECT TERMS WRF, Weather Research and Forecasting, mesoscale modeling, data assimilation, nudging, variational					
16. SECURITY CLASSIFICATION OF:			17. LIMITATION OF ABSTRACT UU	18. NUMBER OF PAGES 76	19a. NAME OF RESPONSIBLE PERSON Brian P Reen
a. REPORT Unclassified	b. ABSTRACT Unclassified	c. THIS PAGE Unclassified			19b. TELEPHONE NUMBER (Include area code) 301-394-3072

Contents

List of Figures	v
List of Tables	vii
Acknowledgments	viii
1. Introduction	1
2. Model Description and Configuration	5
2.1 WRF-ARW	5
2.2 Nudging Data Assimilation	7
2.3 vLAPS Data Assimilation	11
3. Case Description	13
4. Methodology	24
4.1 Observations for Use in Observation Nudging	24
4.2 Obsgrid Analyses	24
4.3 vLAPS Analyses	25
4.4 Creating WRF Input Files	25
5. Experimental Design	29
6. Preliminary Results	32
6.1 Experiment Comparison at Time of Newcastle–Moore Tornado	32
6.1.1 Comparison of Hybrid to Component Techniques	33
6.1.2 Comparison between Varieties of Component Techniques	36
6.1.3 Comparison of Different Cycles	40
6.2 Ability of Hybrid to Simulate Strong Moist Convection	49
7. Summary, Discussion, and Conclusions	54

8. References	57
List of Symbols, Abbreviations, and Acronyms	63
Distribution List	64

List of Figures

Fig. 1	Area covered by the WRF 1-km domain	6
Fig. 2	Winds, heights, and temperature at 500 hPa on 20 May 2013 at 12 UTC from the National Center for Environmental Prediction daily weather maps (http://www.wpc.ncep.noaa.gov/dailywxmap). Barbs are used to show wind (knots), solid lines show isoheights (dekameters above sea level), and dashed lines show isotherms (°C).	14
Fig. 3	Surface analyses of the continental United States from the Weather Prediction Center (http://www.wpc.ncep.noaa.gov/html/sfc2.shtml) for 1200 UTC 20 May 2013	15
Fig. 4	Surface analyses (a,c,e,g,i) of the southern Great Plains from the Weather Prediction Center (http://www.wpc.ncep.noaa.gov/html/sfc2.shtml) and composite base reflectivity (b,d,f,h,j) from Iowa Environmental Mesonet (http://mesonet.agron.iastate.edu/GIS/apps/rview/warnings.phtml) for (a,b) 1200 UTC 20 May 2013, (c,d) 1500 UTC 20 May 2013, (e,f) 1800 UTC 20 May 2013, (g,h) 2100 UTC 20 May 2013, and (i,j) 0000 UTC 21 May 2013	16
Fig. 5	Skew-T's of radiosondes from Norman, Oklahoma, for a) 12 UTC 20 May 2013, b) 18 UTC 20 May 2013, and c) 00 UTC 21 May 2013 (obtained from http://weather.uwyo.edu/upperair/sounding.html). A full wind barb represents 10 kts and a half wind barb represents 5 kts.	21
Fig. 6	Flowchart illustrating creation of the WRF input files for this study. Colored portions of the chart indicate steps required to create WRF initial conditions and boundary conditions of a certain type (HRRR in orange, vLAPS in red, and Obsgrid in blue). The components are labeled with letters to facilitate discussion in the text.	26
Fig. 7	Schematic showing experimental design. t_0 indicates the end of the pre-forecast and the beginning of the forecast, and X will vary among model cycles, but all model cycles end at 00 UTC.....	30
Fig. 8	Composite base reflectivity at 2015 UTC. The black X inside the white square (near the end of the white arrow) indicates the location of the Newcastle–Moore tornado at 2015 UTC. Radar reflectivity obtained from Iowa Environmental Mesonet (http://mesonet.agron.iastate.edu/GIS/apps/rview/warnings.phtml) and cropped to the approximate extent of the WRF-ARW model domain.	33
Fig. 9	WRF-ARW lowest model level radar reflectivity at 2015 UTC on 20 May 2013 for a) HRRR3 ₁₈ , b) VLAPS0 ₁₈ , c) OBSGRID3O ₁₈ , and d) VLAPS3AO ₁₈ . The location of the Newcastle–Moore tornado at 2015 UTC is indicated by the black “X” within the white square (in the same location as marked by the arrow in Fig. 8).	34

Fig. 10	WRF-ARW lowest model level radar reflectivity at 2015 UTC on 20 May 2013 for a) HRRR3 ₁₈ , b) HRRR0 ₁₈ , and c) observed base reflectivity composite. The location of the Newcastle–Moore tornado at 2015 UTC is indicated by the black “X” within the white square. .	37
Fig. 11	WRF-ARW lowest model level radar reflectivity at 2015 UTC on 20 May 2013 for a) VLAPS0 ₁₈ , b) VLAPS1 ₁₈ , c) VLAPS3 ₁₈ , and d) observed base reflectivity composite. The location of the Newcastle–Moore tornado at 2015 UTC is indicated by the black “X” within the white square.	38
Fig. 12	WRF-ARW lowest model level radar reflectivity at 2015 UTC on 20 May 2013 for a) VLAPS3AO ₁₈ , b) VLAPS3A ₁₈ , c) VLAPS3O ₁₈ , and d) observed base reflectivity composite. The location of the Newcastle–Moore tornado at 2015 UTC is indicated by the black “X” within the white square.	40
Fig. 13	WRF-ARW lowest model level radar reflectivity at 2015 UTC on 20 May 2013 for a) HRRR3 ₁₈ , b) HRRR3 ₁₉ , c) HRRR3 ₂₀ , and d) observed base reflectivity composite. The location of the Newcastle–Moore tornado at 2015 UTC is indicated by the black “X” within the white square.	42
Fig. 14	WRF-ARW lowest model level radar reflectivity at 2015 UTC on 20 May 2013 for a) VLAPS3 ₁₈ , b) VLAPS3 ₁₉ , c) VLAPS3 ₂₀ , and d) observed base reflectivity composite. The location of the Newcastle–Moore tornado at 2015 UTC is indicated by the black “X” within the white square.	43
Fig. 15	WRF-ARW lowest model level radar reflectivity at 2015 UTC on 20 May 2013 for a) VLAPS0 ₁₈ , b) VLAPS0 ₁₉ , c) VLAPS0 ₂₀ , and d) observed base reflectivity composite. The location of the Newcastle–Moore tornado at 2015 UTC is indicated by the black “X” within the white square.	45
Fig. 16	WRF-ARW lowest model level radar reflectivity at 2015 UTC on 20 May 2013 for a) OBSGRID3O ₁₈ , b) OBSGRID3O ₁₉ , c) OBSGRID3O ₂₀ , and d) observed base reflectivity composite. The location of the Newcastle–Moore tornado at 2015 UTC is indicated by the black “X” within the white square.	47
Fig. 17	WRF-ARW lowest model level radar reflectivity at 2015 UTC on 20 May 2013 for a) VLAPS3AO ₁₈ , b) VLAPS3AO ₁₉ , c) VLAPS3AO ₂₀ , and d) observed base reflectivity composite. The location of the Newcastle–Moore tornado at 2015 UTC is indicated by the black “X” within the white square.	48
Fig. 18	WRF-ARW lowest model level radar reflectivity at 2015 UTC on 20 May 2013 for VLAPS3AO ₁₈ . The location of the Newcastle–Moore tornado at 2015 UTC is indicated by the black “X” within the small white square. The large white square indicates the area shown in Fig. 19, and the white horizontal line indicates the location of the cross section shown in Fig. 20. Each half barb is 2.5 ms ⁻¹ and each full barb is 5.0 ms ⁻¹	50

Fig. 19	WRF-ARW lowest model level radar reflectivity at 2015 UTC on 20 May 2013 for VLAPS3AO ₁₈ zoomed into the area denoted by the white box in Fig. 18. Each half barb is 2.5 ms^{-1} and each full barb is 5.0 ms^{-1}	51
Fig. 20	Cross section of VLAPS3AO ₁₈ along the white horizontal line in Fig. 18 showing winds in the plane (i.e., the model u- and w-component winds since this cross section is along the model x-dimension), model simulated radar reflectivity (shaded with a thick white line indicating the 0 dBZ isoline and a thin white line indicating the -25 dBZ isoline), and graupel mixing ratio (black contours every 3 g kg^{-1}). The thick black line at the bottom of the plot indicates the portion of the cross section included in Figs. 21 and 22. Each half barb is 2.5 ms^{-1} , each full barb is 5.0 ms^{-1} , and each flag is 25.0 ms^{-1}	52
Fig. 21	Cross section of VLAPS3AO ₁₈ along the portion of the cross section in Fig. 20 indicated by the thick black line along the bottom of that figure. This cross section shows winds in the plane (i.e., the model u- and w-component winds since this cross section is along the model x-dimension), model-simulated radar reflectivity (shaded with a thick white line indicating the 0 dBZ isoline and a thin white line indicating the -25 dBZ isoline), and graupel mixing ratio (black contours every 3 g kg^{-1}). Each half barb is 2.5 ms^{-1} , each full barb is 5.0 ms^{-1} , and each flag is 25.0 ms^{-1}	53
Fig. 22	Cross section of VLAPS3AO ₁₈ along the portion of the cross section in Fig. 20 indicated by the thick black line along the bottom of that figure. This cross section shows model-simulated radar reflectivity (shaded with a thick white line indicating the 0 dBZ isoline and a thin white line indicating the -25 dBZ isoline), and vertical motion (black contours every 5 ms^{-1} with contours representing downward motion dashed). Vertical motion ranges from -16 to $+38 \text{ ms}^{-1}$ in this cross section.	54

List of Tables

Table 1	Experimental design.....	29
---------	--------------------------	----

Acknowledgments

This study was made possible in part due to the data made available to the National Oceanic and Atmospheric Administration by various data providers for inclusion in the Meteorological Assimilation Data Ingest System (MADIS). The Real-Time Mesoscale Analysis use and reject lists provided by Steve Levine at the National Centers for Environmental Prediction's Environmental Modeling Center greatly facilitated making full use of the MADIS observational data set.

1. Introduction

Data assimilation is used in numerical weather prediction (NWP) to incorporate observations into the NWP model to provide a more accurate estimate of the meteorological conditions. There are a wide variety of data assimilation techniques used in NWP, each with its own advantages and disadvantages. Recently, a multitude of combination techniques that aim to leverage the strengths of 2 techniques while minimizing the weaknesses of the individual techniques have emerged. In this study, we propose such a combination data assimilation technique and demonstrate initial results of applying the combination technique to a single case day.

Data assimilation techniques used in NWP include 3-D variational (3DVAR; e.g., Hu et al. 2006; Xiao and Sun 2007), 4-D variational (4DVAR; e.g., Mahfouf et al. 2005; Lopez 2011), Ensemble Kalman filter (EnKF; e.g., Snyder and Zhang 2003; Dowell et al. 2011), and Newtonian relaxation (nudging; e.g., Schroeder et al. 2006; Reen and Stauffer 2010).

In theory, 3DVAR could estimate an optimal analysis for the provided background field and observations. However, since creating an optimal analysis requires perfect knowledge of the background-error covariance and the observation-error covariance, the actual analysis will not be optimal in practice. Background-error covariance is often estimated by using previous NWP simulations or multiple concurrent NWP simulations, and thus 3DVAR is challenging to apply for on-demand forecasts where no previous NWP simulations necessarily exist for the desired domain and computational resources do not allow for multiple concurrent NWP simulations. Without the use of multiple concurrent NWP simulations to calculate the background error covariance, the background error covariance will lack flow dependence. 3DVAR also has the disadvantage that it is an intermittent technique, meaning that an analysis is created and applied at a discrete time. Direct insertion of the analysis at a single time can result in a solution with noise as the model attempts to adjust to a solution that is dynamically consistent with the model's equations. One way to mitigate this is to apply the increment calculated using a 3DVAR analysis over a time period using Incremental Analysis Updating as in Brewster and Stratman (2016) or to analysis-nudge toward the analysis. A weakness of all intermittent data assimilation techniques regards the application of observations made at a time other than the time for which the data assimilation technique is creating an analysis. The effect of these observations cannot be dependent on the difference between the observations and the model state at the time of the observations. First guess at appropriate time (e.g., Lorenc and Rawlins 2005) attempts to mitigate

this by comparing observations to background fields closer in time to the observations, but this is only a rough approximation of a full continuous method since 1) the comparison is either against an analysis or output from a previous model integration and thus is not the current model integration's solution at the observation time (which will be dependent on assimilation of earlier observations), 2) the comparison is limited to the temporally nearest analysis (or temporal interpolation between the nearest analyses), and 3) the effect of the observation is still applied at the analysis time rather than the time of the observation.

4DVAR involves determining a linearized version of the NWP model (e.g., tangent linear model or perturbation forecast model; Lawless et al. 2003) as well as its adjoint and then using these models to allow for forward and backward integration to determine the initial condition analysis that should result in the best forecast over the time period 4DVAR is applied. 4DVAR is basically 3DVAR with a numerical forecast model as strong constraint and the temporal dimension added. Techniques that account for the temporal dimension (i.e., accounting for the temporal variation of observations in creating an analysis at a single time) but do not use the numerical forecast model as a strong constraint are sometimes referred to as 3.5DVAR (e.g., Zhao et al. 2008). While the addition of the temporal dimension in 4DVAR should allow the analysis to incorporate observation information more effectively over a time range than 3DVAR, one challenge involved in using 4DVAR is the very significant computational demands of the method. Also, while 4DVAR could theoretically be implemented by using the full nonlinear forecast model for forward integration and its adjoint (if it exists) for backward integration, because of the computational expense involved in running the full nonlinear forecast model and the difficulty in finding the adjoint, in practice this procedure is often modified. Instead, the full nonlinear forecast model is integrated forward, and this prediction is compared to observations. This prediction is used with a linearized version of the model (tangent linear model) for forward integration and the adjoint of the linearized model for backward integration in an iterative manner to find an updated version of the initial conditions. This iteration is referred to as the inner loop.

In addition to being linearized, the forward model may be coarser and more simplified than the full nonlinear forecast model. The proposed initial conditions arising from the inner loop can then be used to create another solution using the full nonlinear forecast model, which then can have the inner loop applied to it. The repeated use of the full nonlinear forecast model is referred to as the outer loop and is expected to decrease errors resulting from the linearization in the inner loop. However, computational requirements limit the number of integrations of

the outer loop, and thus the linearization and simplification applied in the inner loop can hinder the capability of 4DVAR to fully reach its potential.

EnKF relies on an ensemble of NWP model runs to diagnose the background-error covariance. This allows observations to be assimilated using flow-dependent background-error covariances. EnKF is expensive computationally since by definition multiple NWP simulations must be carried out. Additionally, since a very large number of ensemble members is needed to accurately specify the background-error covariances, techniques (such as localization) must be used to account for the limited number of ensemble members that can be used in practice.

Newtonian relaxation (also known as nudging) involves adding nonphysical terms to the model's tendency terms to gradually nudge the model toward observations or an analysis. Nudging has the advantages that it is a continuous data assimilation method and is not computationally intensive. Additionally, since the parameters used to control the strength of nudging and the spatiotemporal influence of observations are generally set based on past studies, it does not require additional NWP model integrations to specify how the effect of observations are spread for a specific domain or case. However, if resources allow, experiments to improve these parameters could be beneficial. Nudging has the disadvantages that it cannot directly assimilate variables that are not prognostic variables and that it does not fully account for case-specific background-error covariances. A more detailed description of nudging is provided in Section 2.2.

The variational version of the Local Analysis and Prediction System (vLAPS; Jiang et al. 2015) uses a 4-D, multiscale variational scheme (3DVAR) without an actual model constraint for pressure, temperature, wind, and humidity, and uses a modified Barnes scheme with some 1-D variational analysis components (Albers et al. 1996) for other variables. Prior to the introduction of vLAPS, traditional LAPS used the latter approach for all variables. Compared to other variational techniques, vLAPS advantages include the multiscale nature of the technique (in space and time) and its computational efficiency. The multiscale nature of the technique improves the analysis, especially in cases where the background error covariance is not well specified; this is important because it is difficult to accurately determine the background-error covariance (Xie et al. 2011). A more detailed description of vLAPS is provided in Section 2.3.

Various combinations of data assimilation techniques have been implemented. One example is the operational Weather Research and Forecasting (WRF) model-based 9-km Rapid Refresh model, which uses a technique referred to as hybrid ensemble-variational (Benjamin et al. 2016). The method uses 3DVAR but

specifies the background-error covariance as a combination of static background-error covariance and background-error covariance determined from an 80-member ensemble of a coarser global model.

There have been several combination data assimilation techniques that include nudging as one of the techniques. Lei et al. (2012a, 2012b, 2012c) developed a hybrid nudging–ensemble Kalman filter (HNEKF) first in simplified models and then applied it to the Applied Research version of the WRF (Skamarock et al. 2008). This method used an ensemble of WRF simulations to determine both the strength with which observation nudging was applied and the horizontal and spatial spreading of the nudging for each observation. In addition, information from the ensemble was used to allow innovations in one variable to affect another variable (e.g., an error in the u-wind component could result in nudging of the v-wind component). This was applied in a series of 3-h forecasts to produce analyses to force atmospheric transport and dispersion modeling for a single case. The 3-h HNEKF forecasts improved over EnKF in terms of wind direction and over observation nudging in terms of temperature and relative humidity while the performance in the other fields is less conclusive. Lei et al. (2012c) also show that the noise levels in the HNEKF and 4-D data assimilation approaches are much lower than in the EnKF simulation.

The National Center for Atmospheric Research (NCAR) developed a hybrid nudging–ensemble system they refer to as 4D Relaxation Ensemble Kalman Filter (Liu et al. 2015). It uses an ensemble to determine the nudging coefficients used in observation nudging.

Shaw et al. (2008) used 3DVAR to create an analysis to start WRF and then performed observation nudging during the next 3 h. They briefly showed results from a single case suggesting the combination of 3DVAR and nudging performed better than either method separately.

Lei and Hacker (2015) investigated observation nudging, EnKF, and HNEKF in a Lorenz model. Lorenz models involve a much simpler set of equations than NWP models, such as WRF, but include some behaviors reminiscent of the atmosphere; they can be used to test assimilation techniques before application to the much more complex environment of a NWP model. They find that nudging performs better with increasing model error, but the increased model error degrades the covariances used in the hybrid scheme. They conclude that in the Lorenz model they investigated, the hybrid scheme cannot result in errors that are simultaneously lower than both EnKF and observation nudging. In other words, in the Lorenz model for any individual case the hybrid scheme cannot outperform using EnKF alone while also outperforming using observation nudging alone.

However, it is not clear if this conclusion holds for much more complicated models such as WRF. Additionally, even if that hybrid method (HNEnKF) never performs better than both component data assimilation methodologies, the methodology can still be valuable if the hybrid method normally performs better than one of the components and which component performs best varies by case; this can allow the hybrid method to avoid the worst performances of both methods, which might be exactly the cases where it is most important that forecasts be improved. Additionally, this result was specifically for an EnKF observation nudging hybrid and thus is not directly applicable to the combination assimilation methodologies investigated in this study.

This study demonstrates the combination of the vLAPS and nudging data assimilation techniques for a single case day with strong convection. Section 2 describes the Advanced Research version of the WRF model (WRF-ARW) and its configuration here, as well as describing the vLAPS and nudging data assimilation techniques. A description of the case is given in Section 3, Section 4 details the methodology used to carry out the hybrid data assimilation, and Section 5 describes the experimental design. Section 6 describes preliminary results, and Section 7 contains summary and a discussion of the future work.

2. Model Description and Configuration

2.1 WRF-ARW

The Advanced Research version of the Weather Research and Forecasting model (WRF-ARW) V3.6.1 (Skamarock et al. 2008) is applied with 56 vertical layers for an 801×801 1-km horizontal grid spacing domain centered over Oklahoma (Fig. 1).

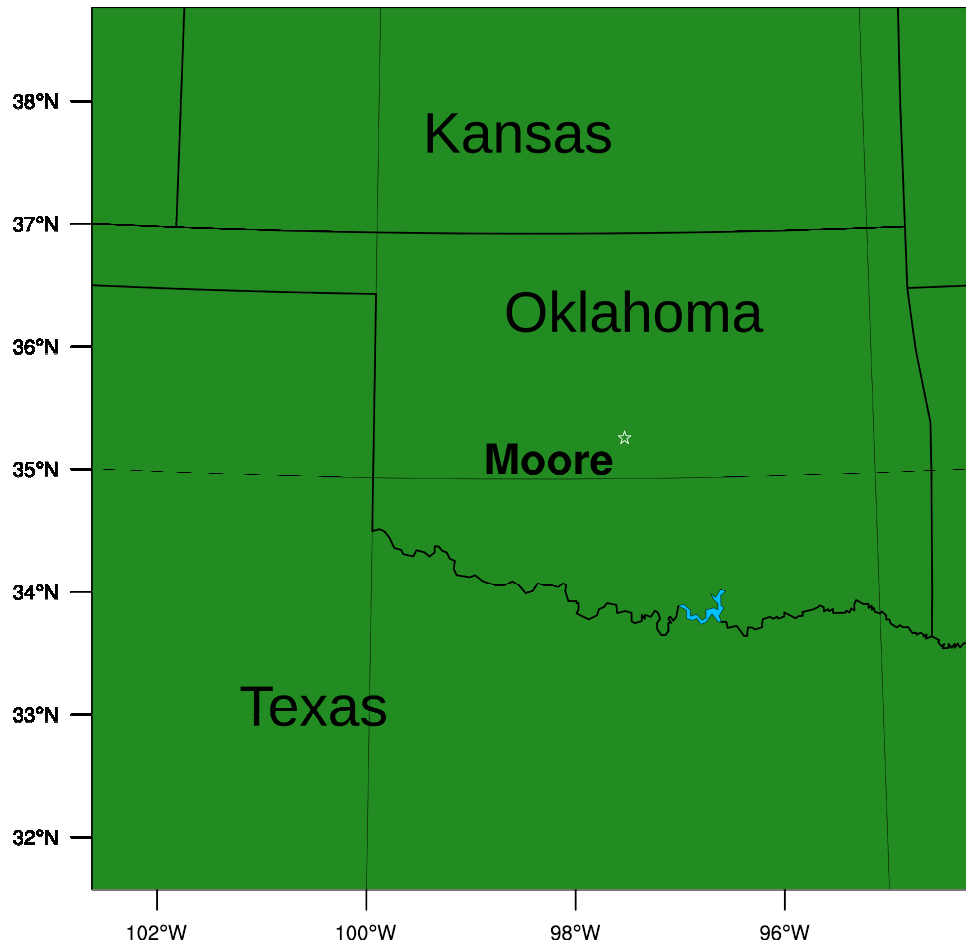


Fig. 1 Area covered by the WRF 1-km domain

WRF-ARW is configured here to use the Mellor-Yamada-Janjić (MYJ) scheme (Janjić 2001) to parameterize the atmospheric boundary layer (ABL). It predicts turbulent kinetic energy (TKE) and is a Mellor-Yamada Level 2.5 turbulence closure model. As in Lee et al. (2012) and Reen et al. (2014), the background TKE is decreased to better simulate conditions with low TKE, and the ABL depth diagnosis is altered.

The Thompson microphysics parameterization (Thompson et al. 2008) is used, but no cumulus parameterization is employed because of the high-resolution nature of the single domain. For radiation, the Rapid Radiative Transfer Model (Mlawer et al. 1997) is used for longwave and the Dudhia scheme (Dudhia 1989) for shortwave. Land surface processes are represented by the Noah land surface model (Chen and Dudhia 2001).

2.2 Nudging Data Assimilation

Nudging (e.g., Stauffer and Seaman 1990; Stauffer et al. 1991), also known as Newtonian relaxation, involves nudging the model toward observations (observation nudging) or analyses (analysis nudging) by adding a term to the tendency equations whose magnitude depends on the magnitude of the difference between the model and either the observation or the analysis. WRF has the ability to nudge toward potential temperature, water vapor mixing ratio, and winds.

Observation nudging (e.g., Stauffer and Seaman 1994; Reen 2016) calculates the difference between an observation and the current model solution at that point (the difference is called the innovation) and then uses the innovation to calculate an additional term for the tendency equation. Observation nudging can be described by the following equation and its description taken directly from Reen (2016):

$$\frac{\partial q \mu}{\partial t}(x, y, z, t) = F_q(x, y, z, t) + \mu G_q \frac{\sum_{i=1}^N W_q^2(i, x, y, z, t) [q_o(i) - q_m(x_i, y_i, z_i, t)]}{\sum_{i=1}^N W_q(i, x, y, z, t)}, \quad (1)$$

where q is the quantity being nudged (e.g., water vapor mixing ratio), μ is the dry hydrostatic pressure, F_q represents the physical tendency terms of q (for water vapor this includes advection, diffusion, conversion from water vapor to cloud water, etc.), G_q is the nudging strength for q , N is the total number of observations, i is the index to the current observation, W_q is the spatiotemporal weighting function based on the temporal and spatial separation between the observation and the current model location, q_o is the observed value of q , and $q_m(x_i, y_i, z_i, t)$ is the model value of q interpolated to the observation location. The quantity $q_o - q_m$ is the innovation; the innovation associated with a given observation evolves with time (both before and after the time of the observation) as the model value (q_m) evolves. Thus, as the model value approaches the observed value, the nudging tendency term decreases.

To apply observation nudging effectively, the observation must be at least somewhat representative of scales represented by the size of the grid cells of the model integration it is being applied to. This should not be problematic in this study because observation nudging has been successfully applied in past studies to horizontal grid spacings much coarser than the 1-km horizontal grid spacing used here. The strength of the observation nudging used here (G_q) is $6 \times 10^{-4} \text{ s}^{-1}$, which means that the e-folding time for the error is approximately 28 min. Thus, assuming that the only nonzero tendency term for the observed value is the observation nudging term, the difference between the model and the observation

after approximately 28 min would be the previous difference divided by e (i.e., $\approx 37\%$ of the previous difference).

The innovation for an observation is not applied at a single time but rather over a time period since the errors at the observation location are correlated with errors nearby in time (the time weighting is included in W_q in Eq. 1). This also allows the model physical tendency terms to dominate, and thus the observations can be assimilated while maintaining a physically consistent solution with a minimum of “noise”. Here, full weighting of above-surface observations is applied for a 1.5-h time period centered on the observation time, and the weighting decreases to zero in the 0.75-h time period on either side of this time period. For surface observations the temporal window is two-thirds as large (full strength for 1.0 h and decreasing to zero in the 0.5 h on either side of this time period) to account for the more rapid atmospheric changes near the surface. The innovation is recalculated frequently throughout the time period over which the innovation is applied so that nudging does not “overshoot” and start nudging the model away from the observation (here it is recalculated every 6 s, which is every other time step).

The innovation is also applied over a horizontal spatial extent since the errors at the observation location are correlated with errors nearby spatially (the spatial weighting is included in W_q in Eq. 1). In general, the innovations are spread horizontally with isotropic weighting functions, with weight decreasing with distance from the observations. Here, a 30-km radius of influence is used at the surface, 60 km just above the surface, and the radius of influence increases with decreasing pressure up to a maximum of 120 km at 500 hPa. Innovations from surface observations are spread along the surface, but the strength at which the innovation is applied is decreased for areas whose model terrain height differs from that at the location of the observation. This is used to limit the spreading of surface observations in a valley to a mountaintop and vice versa.

The vertical spreading of innovations depends on the observation type (the vertical spreading is also included in W_q in Eq. 1). For multilevel observations (e.g., radiosondes), the innovation profile at the location of the observation is interpolated vertically to the model vertical levels at the horizontal location that the innovation is being applied. For single-level above-surface observations (e.g., aircraft observations), the innovation is applied between 50 hPa below and 50 hPa above the observation with the strength at which it is applied decreasing linearly with pressure difference between the observation and the vertical location at which the innovation is being applied. Additionally, the innovations calculated above the top of the model-diagnosed ABL are not applied below the top of the model-diagnosed ABL, and vice versa. For surface observations, in convective

conditions the innovation is applied with full weight throughout the ABL and then ramps down to zero in the next 50 m. In stable conditions the innovation is applied with full weight in the lowest 50 m and then ramps down to zero in the next 50 m.

There are some additional details regarding the observation nudging configuration. The modification of observation nudging of water vapor by Reen et al. (2016) is applied here to prevent excessive drying. At the end of the observation nudging period, we use a 1-h ramp-down period to gradually reduce the observation nudging tendency term to minimize any noise that might be created if the observation nudging tendency terms were suddenly removed. During this ramp-down period, 2 things differ from observation nudging prior to this ramp-down period. First, no new observations (i.e., observations taken during the ramp-down period) are assimilated, thus nudging is toward observations taken prior to the ramp-down period that are not yet too old to be outside the temporal window of that observation. Second, a linear ramp-down weighting factor is multiplied by the other weighting factors to gradually ramp down the observation nudging during this period. An unexpectedly large computational expense was associated with observation nudging in these experiments. Further investigation is needed to determine the causes of this expense. It may be that the large number of model grid cells in the domain (~640,000 per level), compared to most applications of observation nudging, exposed an area where improvements are needed in the implementation of observation nudging in WRF to allow it to better scale to larger domains.

Analysis nudging (e.g., Stauffer and Seaman 1994; Gilliam et al. 2012) calculates the difference between an analysis and the model and then uses that difference (innovation) to construct an additional term for the tendency equations to nudge the model toward the analysis. To apply analysis nudging effectively, the analysis must be representative of the scales resolved by the model domain being nudged toward. If the analysis only resolves scales much coarser than the model domain, then analysis nudging will work to remove the finer-scale structures the model simulates; there is an alternative form of analysis nudging known as spectral nudging that nudges only the large-scale structures (e.g., Vincent and Hahmann 2015). Analysis nudging is usually applied to relatively coarse domains (e.g., Stauffer and Seaman 1994; Rogers et al. 2013; Expósito et al. 2015) since analyses do not normally have sufficient coverage of high-resolution observations to make the analysis representative of finer domains. However, in this study the use of high-resolution data sources in the creation of analyses (as is described later) allow analysis nudging to be applied on the 1-km WRF domain. The

strength of the analysis nudging used here is $3 \times 10^{-4} \text{ s}^{-1}$, which means that the e-folding time for the error is approximately 56 min.

Since analysis nudging is toward an analysis with values at each model grid point at specific time intervals, the temporal and spatial spreading applied differs from that used in observation nudging. The tendency terms added due to analysis nudging are applied at all model time steps during the data assimilation period. Analyses are temporally interpolated to the current time to determine the analysis against which the innovation will be calculated. The analysis nudging innovation is calculated here at each time step. Spatially, each model grid point is generally nudged based on the coincident analysis grid point, although this differs near the surface. WRF analysis nudging also has the capability to limit the strength of analysis nudging in locations where limited nearby observations were included in the analysis; in this study, because of the nature of the analyses, they were assumed to be equally valid at all model grid points.

Here, we nudge both toward surface analyses (surface analysis nudging) and analyses above the surface (3-D analysis nudging). When both surface and 3-D analysis nudging are activated, 1) the surface analyses innovations are applied with full strength throughout the ABL and with 90% of full weight in the layer immediately above the ABL and 2) the above-surface analyses are applied at full strength at all levels above the top of the ABL except at 10% of full weight in the layer immediately above the ABL.

While surface analysis nudging of potential temperature is straightforward, additional details are involved with wind and moisture. For potential temperature, the model's lowest prognostic level temperature is compared to the analysis, and the resulting innovation applied throughout the ABL. Similarity theory is used to adjust the 10-m wind analysis to the lowest model layer (e.g., Stauffer et al. 1991) if the top of the ABL is above the lowest model layer and the lowest model layer where wind is predicted is above 10-m AGL. The adjusted surface wind u and v components are then compared to the model's lowest prognostic level values of u and v , and the resulting innovations applied throughout the ABL. The surface water vapor observation is compared to the model water vapor at each model prognostic layer in the ABL (and one layer above), and the resultant innovation applied to that same level.

At the end of the analysis nudging period, we use a 15-min time period to ramp down the influence of the analysis nudging. During this time period, the model is nudged toward the analysis valid at the beginning of this time period, and the weighting decreases linearly with time to zero. Although the standard version of WRF V3.6.1 does not nudge toward the analysis valid at the beginning of the

ramp-down time period because of a bug, the bug was fixed in the version of WRF V3.6.1 used for this study (the bug fix was also submitted to the WRF developers and included in the public release version of WRF starting in WRF V3.8).

2.3 vLAPS Data Assimilation

LAPS was developed by the National Oceanic and Atmospheric Administration (McGinley et al. 1991) and traditionally used a modified Barnes analysis (Hiemstra et al. 2006) with some 1-D variational components (Albers et al. 1996). The vLAPS retains the traditional techniques for some variables but moves to a 3-D, multiscale variational scheme (3DVAR) for pressure, temperature, winds, and humidity (Jiang et al. 2015). Some of the vLAPS description in this section is from Jiang et al. (2015).

The 3DVAR scheme used in vLAPS is based on the Space and Time Multiscale Analysis System (Xie et al. 2011). Even though it does not have a forecast model as a constraint like a 4DVAR, it indeed considers temporal information with a half-hour analysis time window. The multiscale approach pioneered in computational mathematics applications (see Briggs 1987) was adopted by Xie et al. (2011) for meteorological and oceanographic data assimilation and improves accuracy and computational efficiency compared to nonmultiscale variational techniques. vLAPS applies the multiscale technique spatially and temporally.

Spatially, vLAPS completes a 3DVAR analysis on a coarse grid, and the output of that analysis is used as the background for a 3DVAR analysis at a finer scale; this process continues until the analysis is at an adequate resolution. For each grid, a Laplacian function of the difference between analysis and background is added to the cost function to mimic the background term of a 3DVAR, which determines the spreading of the influence of an observation. The coefficients multiplying the Laplacian terms control the influence radius of observations. The use of a Laplacian rather than a recursive filter has the benefit of better retaining the gradients of the background to fit the observations. Since vLAPS reduces the coefficients of the Laplacian terms in the cost function when moving from a coarser grid to a finer one, the effective radius of influence of an observation decreases as the horizontal grid spacing of the analysis decreases. Performing the analysis at multiple spatial scales allows the influence of observations in data-sparse areas to spread broadly in coarser grids while keeping the fine-scale features resolvable in data-rich areas in finer grids. This also makes the technique less dependent on accurate background error covariance. Here, the coarsest grid used for the analysis has 16-km horizontal grid spacing and 50-hPa vertical grid

spacing; each subsequent analysis decreases the horizontal and vertical grid spacing in half until this division is stopped if the grid space exceeds the smallest spacing specified by the user. For this case, we set 25 hPa for the vertical. This, the finest analysis grid, uses 2 km horizontal grid spacing and 25 vertical grid spacing. Five analyses were completed, including the coarsest and finest resolution analyses.

The surface analysis is completed separately from the analysis for layers above the surface, and the surface analysis lacks a vertical component.

Temporally, vLAPS uses multiple time frames to create the analysis at an individual analysis time; this allows extraction of information from frequent observations (e.g., from radars) related to rapid changes. A time filter is used to weigh the contributions of observations nearer to the analysis time more strongly than observations farther in the past or future. The time filter used is a Laplacian filter. As with the spatial dimension, the analysis is repeated multiple times with increasingly short temporal windows in which observations can affect the analysis. In this case, this results in the longest temporal window being 30 min, and the shortest being 15 min, both centered on the analysis time. Note that the spatial and temporal refinement of the analyses are taking place simultaneously (i.e., the first analysis is coarse spatially and temporally, the next analysis is finer spatially and temporally). For observations that are not taken at the time of one of the first-guess analyses, the first-guess analyses are temporally interpolated to the observation to determine the difference between the observation and the analyses.

The multiscale approach of vLAPS is related to other data assimilation approaches. For example, it is similar to a 4DVAR approach, but instead of using the full NWP model as a constraint, vLAPS uses a time filter and other simplified constraints. The simplified constraints vLAPS used include geostrophic and hydrostatic balances as weak constraints and incompressibility as a strong constraint. It is also similar to ensemble-variational data assimilation (4DEnVar), wherein ensemble covariances are used for temporal constraints (Liu et al. 2008).

The vLAPS variational assimilation differs significantly from the 3DVAR in the widely used Gridpoint Statistical Interpolation (GSI) package. In addition to the multigrid technique, for control variables vLAPS uses the u- and v-wind components (Xie and MacDonald 2011), whereas GSI uses stream function and velocity potential. Xie et al. (2002 and 2011) demonstrate that the use of the latter 2 for control variables is undesirable; this is especially true for convective-scale resolutions. There are several other advantages of vLAPS, such as better use of physical balances, hot-start, more efficient storage of the background covariances,

nonlinear minimization compared to GSI's linearized minimization, and better representation of observation errors.

The cloud analysis technique applied here was first described in Albers et al. (1996). Geostationary Operational Environmental Satellite (GOES) data (infrared + visible), radar, surface observations (METARs), and model first-guess fields are combined in the so-called “traditional” or sequential cloud analysis. A preliminary analysis is constructed of cloud fraction using model first-guess humidity and METAR reports that are spread horizontally. Next, infrared satellite data are added in a series of cloud-clearing and cloud-building steps, with similar steps for visible satellite data. Finally, radar data are added to complete the 3-D cloud fraction analysis. This cloud field is postprocessed into 3-D hydrometeor fields and associated vertical velocity to feed back into the dynamical fields (namely, the 3-D wind). A variational cloud analysis is under development for future use.

3. Case Description

To demonstrate the potential utility of the combined data assimilation technique proposed here, we investigate a single case day (20 May 2013) with strong convection in the southern Great Plains region. At 12 Coordinated Universal Time (UTC) at 500 hPa (Fig. 2), an upper-level low was centered over the northern Great Plains with the axis of the trough to the southwest. This resulted in approximately 50-kt ($\approx 26 \text{ ms}^{-1}$) flow from the west-southwest over Oklahoma and eastern Kansas at 500 hPa.

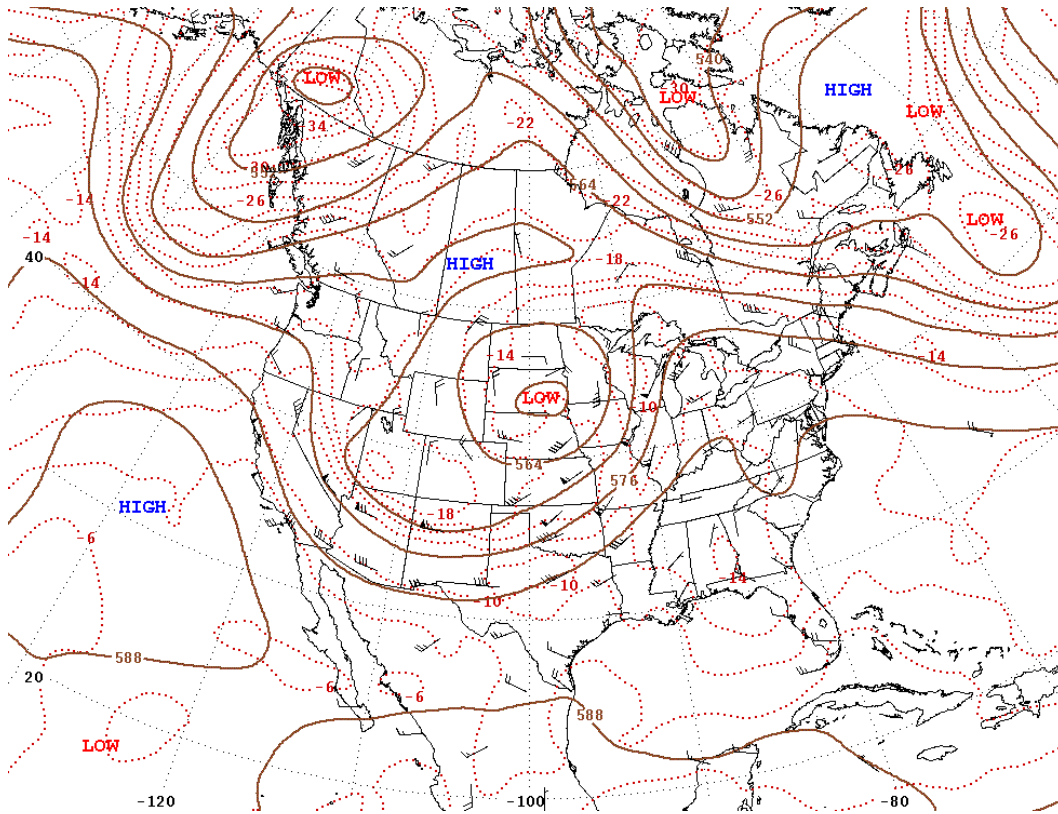


Fig. 2 Winds, heights, and temperature at 500 hPa on 20 May 2013 at 12 UTC from the National Center for Environmental Prediction daily weather maps (<http://www.wpc.ncep.noaa.gov/dailywxmap>). Barbs are used to show wind (knots), solid lines show isoheights (dekameters above sea level), and dashed lines show isotherms (°C).

At the surface, at 12 UTC (Fig. 3) a cold front extended south from the northern Great Plains but transitioned to a stationary front over Kansas and Oklahoma and curved more westerly, with a dry line extending south from the front over west Texas. Observations (Fig. 4a) indicate a strong moisture contrast near the front in southern Oklahoma and northern Texas at 12 UTC, with much drier conditions on the northwest side of the front. Precipitation at 12 UTC (Fig. 4b) is limited to a broken swath oriented west–southwest to east–northeast from far northern Texas through northern Oklahoma and southern Kansas. As diurnal heating progresses, the frontal position and moisture gradient remain similar through 15 UTC (Fig. 4c) and 18 UTC (Fig. 4e) with the weak line of precipitation becoming more continuous and oriented southwest to northeast mostly over Kansas (Fig. 4e–f).

By 2100 UTC a dry line is analyzed south from near the front in central Oklahoma (Fig. 4g) with a line of strong convection in place through central Oklahoma and southeastern Kansas (Fig. 4h). At 0000 UTC the surface analysis (Fig. 4i) indicates frontal placement is similar, but now analyzed as a cold front,

and a squall line is analyzed across southeastern Oklahoma, which is consistent with the radar observation at this time (Fig. 4j).

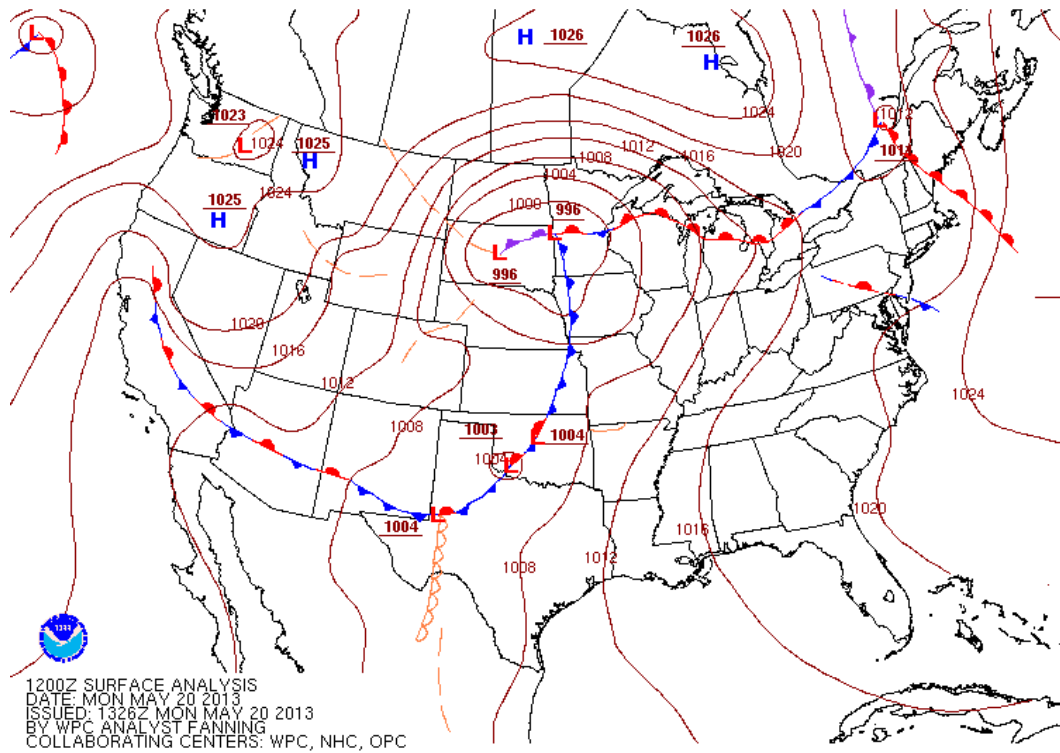


Fig. 3 Surface analyses of the continental United States from the Weather Prediction Center (<http://www.wpc.ncep.noaa.gov/html/sfc2.shtml>) for 1200 UTC 20 May 2013

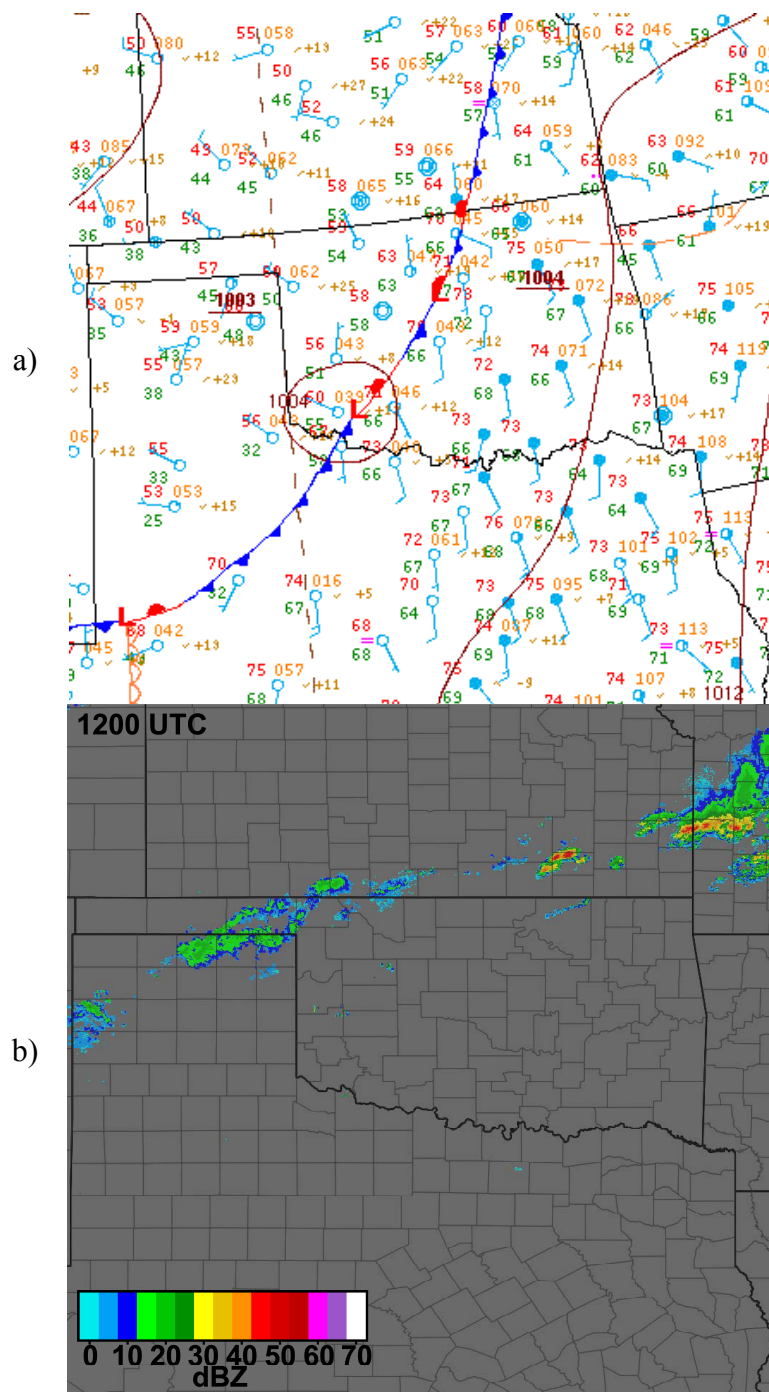


Fig. 4 Surface analyses (a,c,e,g,i) of the southern Great Plains from the Weather Prediction Center (<http://www.wpc.ncep.noaa.gov/html/sfc2.shtml>) and composite base reflectivity (b,d,f,h,j) from Iowa Environmental Mesonet (<http://mesonet.agron.iastate.edu/GIS/apps/rview/warnings.phtml>) for (a,b) 1200 UTC 20 May 2013, (c,d) 1500 UTC 20 May 2013, (e,f) 1800 UTC 20 May 2013, (g,h) 2100 UTC 20 May 2013, and (i,j) 0000 UTC 21 May 2013

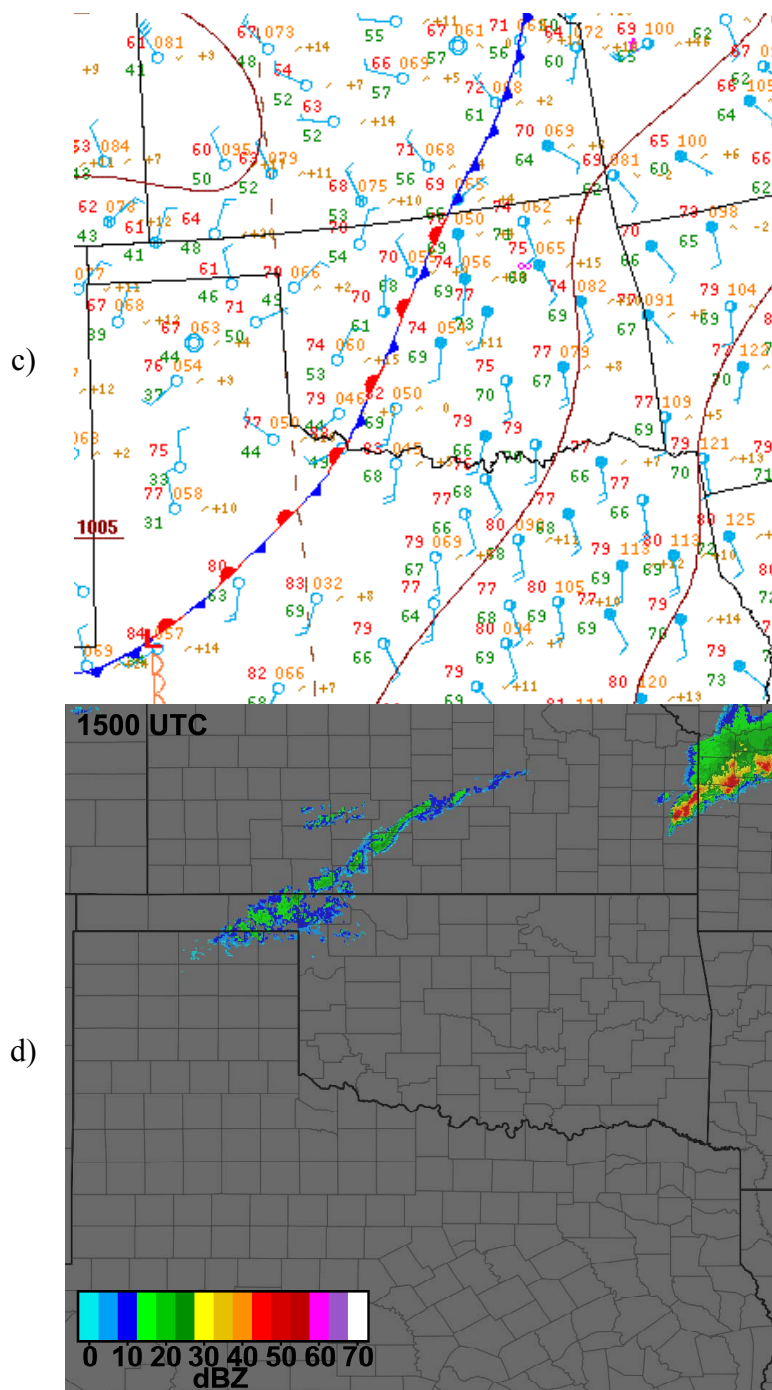


Fig. 4 Surface analyses (a,c,e,g,i) of the southern Great Plains from the Weather Prediction Center (<http://www.wpc.ncep.noaa.gov/html/sfc2.shtml>) and composite base reflectivity (b,d,f,h,j) from Iowa Environmental Mesonet (<http://mesonet.agron.iastate.edu/GIS/apps/rview/warnings.phtml>) for (a,b) 1200 UTC 20 May 2013, (c,d) 1500 UTC 20 May 2013, (e,f) 1800 UTC 20 May 2013, (g,h) 2100 UTC 20 May 2013, and (i,j) 0000 UTC 21 May 2013 (continued)

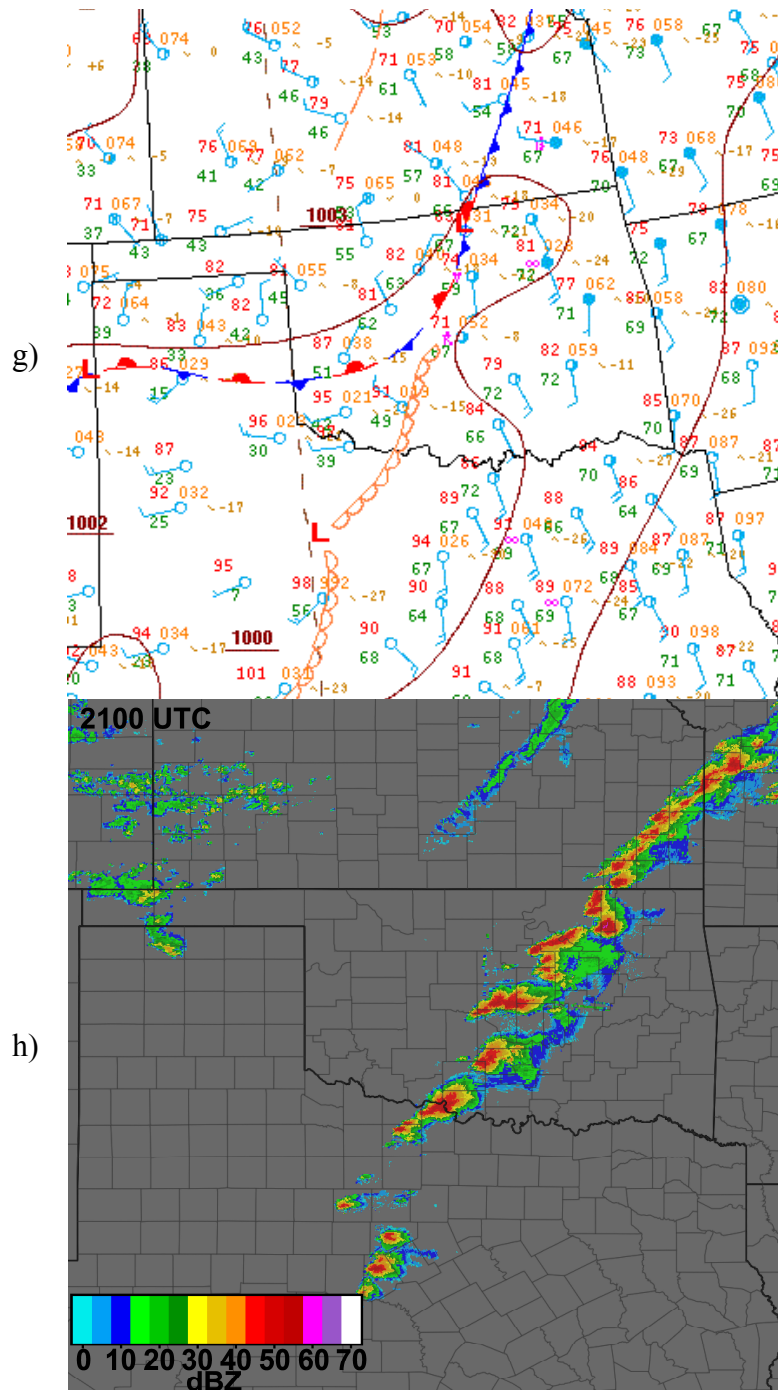


Fig. 4 Surface analyses (a,c,e,g,i) of the southern Great Plains from the Weather Prediction Center (<http://www.wpc.ncep.noaa.gov/html/sfc2.shtml>) and composite base reflectivity (b,d,f,h,j) from Iowa Environmental Mesonet (<http://mesonet.agron.iastate.edu/GIS/apps/rview/warnings.phtml>) for (a,b) 1200 UTC 20 May 2013, (c,d) 1500 UTC 20 May 2013, (e,f) 1800 UTC 20 May 2013, (g,h) 2100 UTC 20 May 2013, and (i,j) 0000 UTC 21 May 2013 (continued)

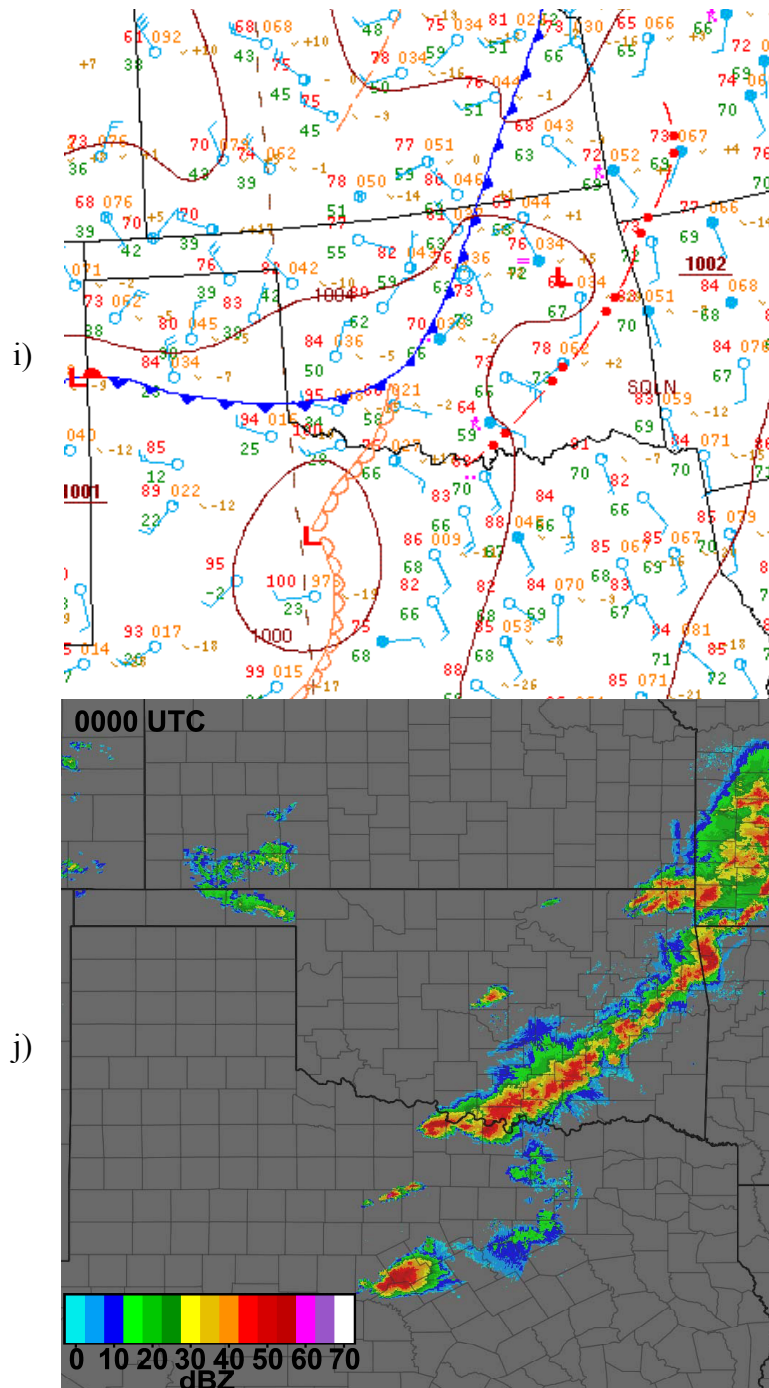


Fig. 4 Surface analyses (a,c,e,g,i) of the southern Great Plains from the Weather Prediction Center (<http://www.wpc.ncep.noaa.gov/html/sfc2.shtml>) and composite base reflectivity (b,d,f,h,j) from Iowa Environmental Mesonet (<http://mesonet.agron.iastate.edu/GIS/apps/rview/warnings.phtml>) for (a,b) 1200 UTC 20 May 2013, (c,d) 1500 UTC 20 May 2013, (e,f) 1800 UTC 20 May 2013, (g,h) 2100 UTC 20 May 2013, and (i,j) 0000 UTC 21 May 2013 (continued)

The 1200 UTC radiosonde at Norman, Oklahoma (Fig. 5a), indicates a thin saturated layer at approximately 900 hPa at the base of a strong capping inversion and then a deep elevated mixed layer. At 1800 UTC (Fig. 5b), daytime heating along with the formation of a convective boundary layer and a weakened capping inversion are present; the convective available potential energy at this time is 3135 J kg^{-1} . By 0000 UTC, the main line of convection is southeast of Norman, but an isolated cell is at least in the vicinity of Norman (Fig. 4j), and there is a shallow isothermal layer at the surface topped by an inversion (Fig. 5c). Also, note the backing in the near-surface wind between 1800 and 0000 UTC (compare Fig. 5c to Fig. 5b), and the speed shear present in the 1800 and 0000 UTC radiosondes.

A total of 42 tornadoes were reported in the United States on 20 May 2013, including 18 in Oklahoma, 11 in Missouri, 5 in Texas, 3 in Kansas, and 3 in Arkansas (NCEI 2016). An EF5 touched down at 1956 UTC in Newcastle, Oklahoma, and traveled through Moore, Oklahoma, before dissipating approximately 2035 UTC (Atkins et al. 2014; Burgess et al. 2014; Kurdzo et al. 2015).

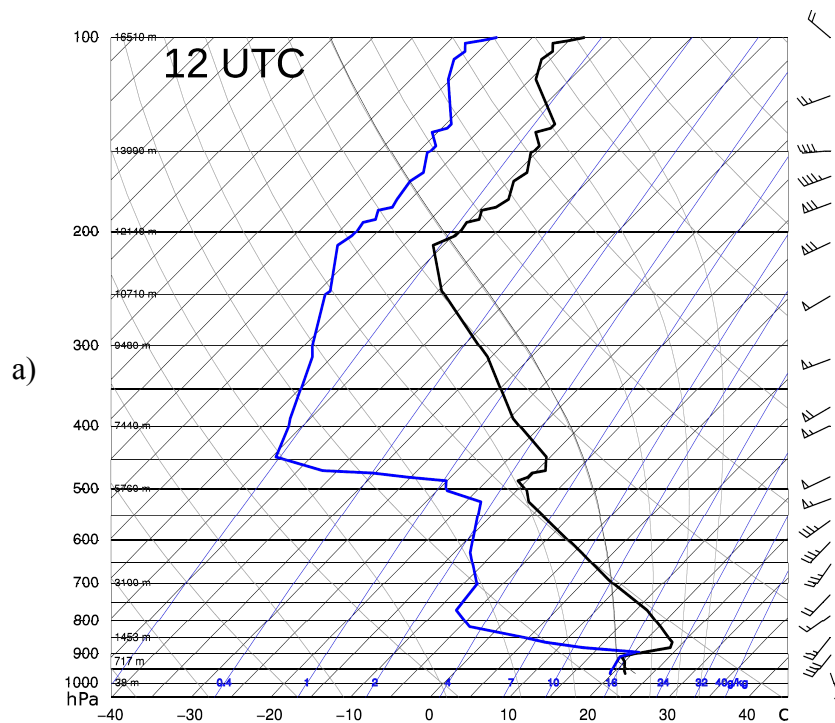


Fig. 5 Skew-T's of radiosondes from Norman, Oklahoma, for a) 12 UTC 20 May 2013, b) 18 UTC 20 May 2013, and c) 00 UTC 21 May 2013 (obtained from <http://weather.uwyo.edu/upperair/sounding.html>). A full wind barb represents 10 kts and a half wind barb represents 5 kts.

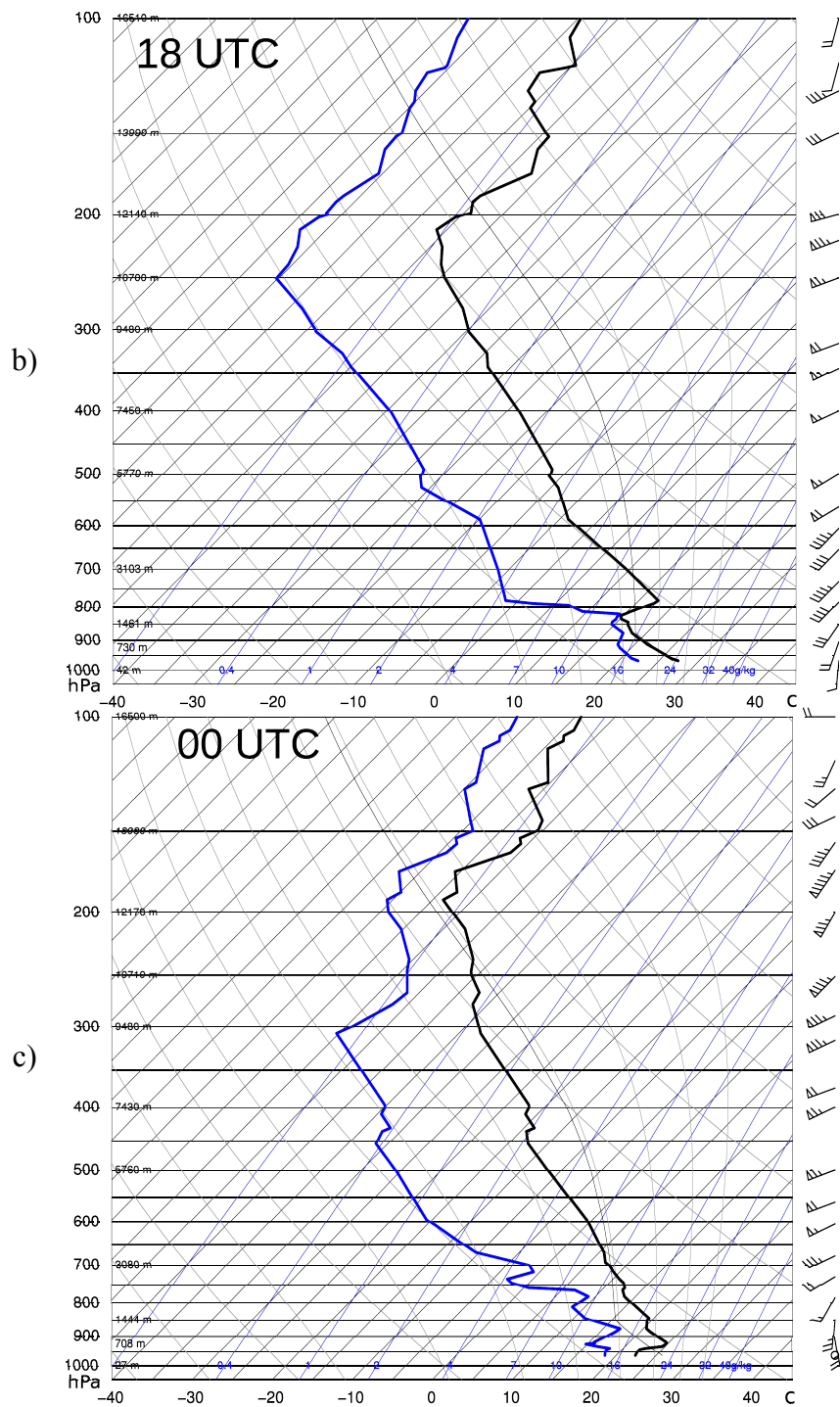


Fig. 5 Skew-T's of radiosondes from Norman, Oklahoma, for a) 12 UTC 20 May 2013, b) 18 UTC 20 May 2013, and c) 00 UTC 21 May 2013 (obtained from <http://weather.uwyo.edu/upperair/sounding.html>). A full wind barb represents 10 kts and a half wind barb represents 5 kts (continued).

Hanley et al. (2016) employed the United Kingdom Met Office's Unified Model with 4.4/2.2/0.5/0.2/0.1-km horizontal grid spacing nests to investigate the 20 May 2013 Moore tornado. They used no data assimilation (data assimilation was applied to the global model driving the outermost nest). Their 2.2-km grid initiates convection at about the correct time in the Oklahoma City area and simulates supercells, but convection persists too long in this area. Their 200- and 100-m grids simulate tornado-like vortices, but do so approximately 2.5 h later than the observed Moore tornado.

Zhang et al. (2015, 2016) examined predictability of the convection on 20 May 2013 using WRF-ARW. Zhang et al. (2015) used nested 27-, 9-, 3-, and 1-km horizontal grid spacing domains to investigate the impact on the simulation of convection from temporal variations in initial conditions and from horizontally shifting the underlying terrain. They find that temporal shifting of initial conditions generally temporally shifts convection as expected but in some cases does not affect convective timing because the lateral boundary conditions are controlling convective initiation. The temporal shifting impacts the paths of some supercells (diagnosed via updraft helicity) much more than others, suggesting that the predictability of some supercells is larger than other supercells. Terrain shifting changed the timing of convective initiation, as well as how the storms developed. Zhang et al. (2016) also use nested 27-, 9-, 3-, and 1-km horizontal grid spacing domains, but add a 250-m nest to create perturbations to create a 60-member, 1-km ensemble to investigate predictability. The magnitude of these perturbations is unobservable with current observing platforms, thus the ensemble represents the effects of currently unavoidable observational uncertainty. Zhang et al. (2016) find that while a line of storms is produced in all of the ensemble members, the details of individual storms in that line differ among the ensemble members; this suggests that the line of storms is predictable but details along that line of storms may not be predictable at this time.

Snook et al. (2016) produced 500-m horizontal grid spacing Advanced Regional Prediction System (ARPS) simulations to investigate numerical weather prediction forecasts of hail for this case. They applied EnKF using 40 ensemble members with radar reflectivity, radar radial velocity, and surface observations assimilated every 5 min between 1830 and 1930 UTC, followed by a 90-min forecast (1930–2100 UTC). Their results indicated that for this case the model had skill at predicting hail.

4. Methodology

This study investigates 3 methods to produce initial conditions as well as the application of analysis and observation nudging. This section describes the methodology used to create the initial conditions as well as the analyses and observations that are nudged toward.

4.1 Observations for Use in Observation Nudging

The observations used for observation nudging data assimilation were obtained from the Meteorological Assimilation Data Ingest System (MADIS; <https://madis.noaa.gov/>). The specific MADIS data sources applied here are standard surface, mesonet surface, profiler, radiosonde, and Aircraft Communications Addressing and Reporting System (ACARS) observations. After simulations were complete, we discovered that a software error resulted in profiler and ACARS observations not being included at 13, 19, and 21 UTC.

Quality control is applied using 3 resources. First, the quality control flags attached to the MADIS data set are used to remove observations marked as problematic. Second, use/reject lists that were designed for the Real-Time Mesoscale Analysis (De Pondeca et al. 2011) are applied only to the surface mesonet observations; these lists are designed to deal with the data quality issues that can be more prevalent in the mesonet observations (e.g., poor siting) than in standard surface observations. Third, the Obsgrid program (NCAR 2016) is used to apply quality control based on evaluating observations against a first-guess field and against nearby observations (buddy check). The first-guess fields we use are from the 15 UTC cycle of the 3-km High-Resolution Rapid Refresh model (HRRR; Alexander et al. 2013; <http://rapidrefresh.noaa.gov/hrrr>) on 20 May 2013. Obsgrid performs quality control of temperature, wind, relative humidity, sea-level pressure, and surface pressure (NCAR 2016; Reen 2015). In this study, the first-guess field (HRRR) is vertically interpolated to additional pressure levels to facilitate quality control of single-level above-surface observations (ACARS data) and allow for additional vertical structure to be retained in multilevel observations (e.g., radiosonde) data.

4.2 Obsgrid Analyses

Obsgrid produced an objective analysis used as initial conditions for some simulations. The analysis combines the observations in Section 4.1 with 3-km HRRR fields from the 15 UTC cycle on 20 May 2013. Obsgrid was configured here to perform multiscan Cressman analyses of temperature, wind, relative humidity,

and surface pressure. The surface pressure analysis is used to determine how the surface analyses of the other fields are applied in the WRF initial conditions based on the difference between the WRF surface pressure and the surface pressure of the Obsgrid analyses. The Cressman analyses for wind and relative humidity are flow dependent. Five scans are applied using the default Obsgrid technique of determining radius of influence based on assuming an average of 325 km between upper air observations. This results in radii of influence of 520, 354, 255, 179, and 126 km for above-surface observations. Surface observations are assumed to have a 40% smaller radii of influence, given the greater degree of spatial heterogeneity at the surface; however, Obsgrid limits the radii of influence for surface observations specified as a percentage of the radius of influence of the upper-air observations to be between 4.5 and 100.0 model grid cells. The resulting surface radii of influence for the 5 scans are 100, 70, 49, 34, and 24 km.

4.3 vLAPS Analyses

For this case 15-min vLAPS analyses were created using the 3-km HRRR fields from the 15 UTC cycle on 20 May 2013. One source of observations used in the analysis was the MADIS data set. The observation types obtained from the MADIS data set included standard surface, mesonet surface, profiler, radiosonde, and ACARS. Pilot observations were obtained from the Federal Aviation Administration reporting sky cover, turbulence, wind direction, and icing. In addition to using the MADIS quality control flag, vLAPS also checks observations against the background field to determine if the difference is large enough that the observation should be omitted from the analysis. Radial velocity from 26 radars (WSR-88D and Terminal Doppler Weather Radar) were ingested using the variational data assimilation, but the reflectivity was ingested using the earlier nonvariational LAPS. The LAPS cloud analysis uses GOES imagery data to remove clouds where GOES indicates that clouds are not present. The LAPS cloud analysis also uses radar, surface observations (METARs), and model first-guess fields and uses these to provide 3-D hydrometeor content; the results of the cloud analysis also are used to adjust the 3-D wind field. Among the fields analyzed by LAPS are temperature, water vapor, winds, and hydrometeors.

4.4 Creating WRF Input Files

The process of creating the WRF-ARW input files for the various experiments described in Section 5 is somewhat involved (Fig. 6). In the following description, a letter in brackets is used to signify the component labeled with that letter in the figure. Most of the components are standard WRF Preprocessing System (WPS) software, or altered versions of the standard preprocessors.

In the first step, static geographical data (e.g., terrain height, soil type) are ingested by Geogrid [A] to create static geographical data for the current domain (geo_em*). The hourly 3-km HRRR data from the 15 UTC cycle on 20 May 2013 is then converted from Gridded Binary (GRIB) format into WRF intermediate-format files by both the standard version of Ungrib [E] and a “high-resolution” version of Ungrib [B]. The standard version of Ungrib [E] retains data on all of the pressure levels present in the original GRIB file and does not add data on additional pressure levels. The high-resolution version of Ungrib [B] differs from the standard version in that it vertically interpolates the HRRR data to additional pressure levels to allow for improved quality control of single-level above-surface observations and to better retain vertical resolution of multilevel observations. When observations are quality controlled (at a later step), single-level above-surface observations (e.g., aircraft data) are quality controlled against the nearest pressure level. By interpolating the HRRR data to additional pressure levels, the quality control of these observations can use HRRR-derived data closer to the pressure level of the observation. When multilevel observations (e.g., radiosondes) are quality controlled (at a later step), they are vertically interpolated to the pressure levels of the HRRR-derived data to allow quality control of the observations against the HRRR data. By interpolating the HRRR data to additional pressure levels, a more detailed vertical structure can be retained in multilevel observations. The intermediate files created by both versions of Ungrib ([B] and [E]) are ingested by Metgrid ([C] and [F], respectively) to create HRRR data gridded to the WRF domain’s horizontal grid (met_em* files).

The met_em* files originating from the Metgrid [C] run using output from the high-resolution version of Ungrib [B] are ingested by Obsgrid [D] along with MADIS observations. These met_em* files contain the pressure levels in the original HRRR data, but also include additional pressure levels onto which the HRRR data are interpolated. Obsgrid performs quality control of the MADIS observations by comparing each MADIS observation to nearby observations and to the HRRR data in the met_em* files with the additional pressure levels. The quality controlled observations are output in WRF observation nudging format as OBS_DOMAIN* files ready for WRF [Q] to ingest for observation nudging.

The met_em* files originating from the Metgrid [F] run using output from the non-high-resolution version of Ungrib [E] are used for creating initial conditions and boundary conditions. These met_em* files retain the pressure levels in the original HRRR data. The subsequent processing of these met_em* files differs depending on which type of initial conditions are being generated.

To create Obsgrid-based initial conditions the met_em* files from Metgrid [F] are used as the first guess for an objective analysis created by Obsgrid [H] by

combining the HRRR-based met_em* files with the MADIS observations. The resultant objective analyses (meteo_em*) then have snow-cover-related fields removed to avoid potential discrepancies with vLAPS-based initial conditions that do not have snow cover as a field. (Snow cover here refers to a yes/no flag indicating snow cover and is separate from snow depth. Snow cover is not processed in the standard WPS/WRF software but was added in the US Army Research Laboratory [ARL] implementation to allow snow cover fields to be ingested and thus improve snow characterization in WRF simulations.) The objective analyses file for the initial time (meteo_em* from [I]) and the HRRR-based met_em* with snow cover removed (met_em* from [G]) are then processed by the WRF component Real to create initial condition (wrfinput*) and boundary condition (wrfbdy*) files for WRF that are on the WRF vertical levels.

The simplest of the initial conditions to create are those that are based solely on the HRRR output and thus use no observations. To create HRRR-based initial conditions, Real [K] creates initial condition (wrfinput*) and boundary condition (wrfbdy*) files on the WRF vertical levels using the met_em* files from Metgrid [F] with snow cover removed [G].

To create the vLAPS-based WRF initial conditions, the vLAPS analyses are ingested by Metgrid [N] to create vLAPS-based met_em* files. Real [O] is then used to create initial condition files (wrfinput*), which are renamed wrfvar_output* for input into da_update_bc [L]. The WRF input and boundary condition files created by Real [K] from the HRRR-based met_em* files are also input to da_update_bc [L]. This program [L] updates the boundary conditions in wrfbdy* based on the differences between the initial conditions from which these boundary conditions were created (wrfinput*) and the initial conditions that will actually be used (wrfvar_output*). This prevents a mismatch near the boundary between the boundary condition and initial condition file. The boundary condition updating program (da_update_bc [L]) creates an updated boundary condition file (wrfbdy*) ready for ingestion by WRF [Q], as well as an initial condition file wrfvar_output* that we rename wrfinput*. This vLAPS-based initial condition file does not contain the HRRR soil moisture and soil temperature fields, nor the netCDF file “global attributes”. Therefore, we use the tool NetCDF Operators (<http://nco.sourceforge.net/>) component ncks [M] to take the soil moisture, soil temperature, and global attributes from the HRRR-based initial conditions (the wrfinput* created by Real [K]) and place them in the vLAPS-based initial conditions (wrfinput*, which is the wrfvar_output* files output by da_update_bc [L]). The resultant initial condition file is the vLAPS wrfinput* file used by WRF [Q].

In addition to the observation nudging file (OBS_DOMAIN*) and the initial and boundary conditions (wrfinput* and wrfbdy*), we must also produce surface and 3-D analysis nudging files. These are created from the vLAPS-based met_em* files created by Metgrid [N]. Applying Real [O] to these files creates the 3-D analysis nudging files (wrffdda*). Using Obsgrid [P] on these met_em* files without providing observations to Obsgrid [P] creates vLAPS-based surface analysis nudging files (wrfsfdda*) ready for ingestion by WRF [Q].

5. Experimental Design

A series of experiments (Table 1; Fig. 7) were carried out to investigate the potential value of combining the vLAPS and nudging data assimilation techniques. The experiments differed in their initial conditions (HRRR, vLAPS, or Obsgrid), the length of pre-forecast applied (0, 1, or 3 h), and whether observation or analysis nudging was applied. The pre-forecast is used to refer to a period at the beginning of the model integration during which 1) observations are assimilated or 2) the model is assumed to be spinning up. Assimilation of observations taken during the pre-forecast may extend into the beginning of the free forecast, but no observations valid during the free forecast should be assimilated. However, the analyses being analysis nudged toward here include observations valid during the beginning of the forecast period (first 30 min for Obsgrid analyses and 15 min for vLAPS analyses). The experiments' names start with text indicating the initial condition source ("HRRR", "VLAPS", or "OBSGRID"), then the length of the pre-forecast in hours (single integer), followed by "O" if observation nudging is applied, and "A" if analysis nudging is applied.

Table 1 Experimental design

Assimilation	Name	Initial Condition Source	Pre-forecast Length (h)	Nudging	
				Analysis	Obs
None	HRRR0	HRRR	0	N	N
None	HRRR3	HRRR	3	N	N
vLAPS	VLAPS0	VLAPS	0	N	N
vLAPS	VLAPS1	VLAPS	1	N	N
vLAPS	VLAPS3	VLAPS	3	N	N
Obsgrid/Nudging	OBSGRID3O	OBSGRID	3	N	Y
Partial hybrid	VLAPS3O	VLAPS	3	N	Y
Partial hybrid	VLAPS3A	VLAPS	3	Y	N
Full hybrid	VLAPS3AO	VLAPS	3	Y	Y

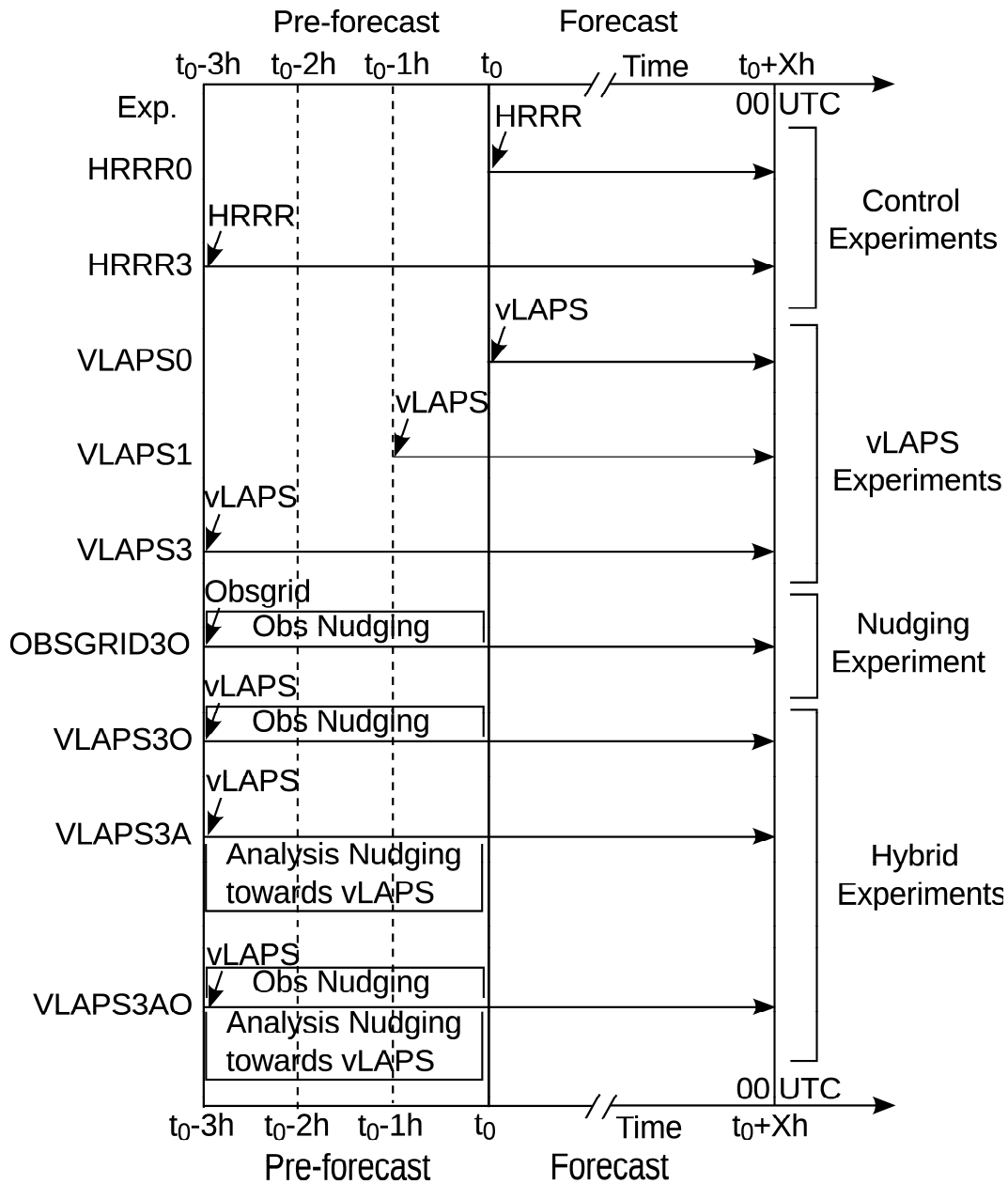


Fig. 7 Schematic showing experimental design. t_0 indicates the end of the pre-forecast and the beginning of the forecast, and X will vary among model cycles, but all model cycles end at 00 UTC.

The first experiment (HRRR0) serves as a control experiment. It uses HRRR to determine initial and boundary conditions and uses neither a pre-forecast nor nudging. HRRR3 is similar but includes a 3-h model spin-up time period to investigate the potential benefit of a 3-h pre-forecast even if no data assimilation is applied. This will also facilitate evaluation of other experiments and whether differences between experiments are due to a 3-h data assimilation period or simply due to starting the model integration 3 h earlier.

The second set of experiments (VLAPS0, VLAPS1, and VLAPS3) uses the vLAPS analysis as the initial condition and uses either no pre-forecast spin-up period (VLAPS0), a 1-h pre-forecast spin-up period (VLAPS1), or a 3-h pre-forecast spin-up period (VLAPS3). The VLAPS0 experiment most closely matches applications of the vLAPS technique in past studies, but the other 2 experiments are added here to determine the potential benefit and preferred length of a spin-up period; VLAPS3 also facilitates comparison with nudging experiments wherein nudging is applied over 3 h.

OBSGRID3O uses an objective analysis created by Obsgrid (see Section 4.2) as initial conditions for WRF and then applies observation nudging also created via Obsgrid (see Section 4.1) over the first 3 h. OBSGRID3O matches the data assimilation methodology commonly used at ARL.

The final 3 experiments combine vLAPS analysis with nudging. VLAPS3O uses vLAPS to specify the initial conditions and then applies observation nudging over the first 3 h. VLAPS3A also uses vLAPS to specify the initial conditions, but also analysis nudges toward 15-min vLAPS analyses during the first 3 h (it does not apply any observation nudging). VLAPS3AO is the full hybrid experiment wherein vLAPS analysis are used to specify the initial conditions and are nudged toward during the first 3 h, but the model solution is also observation nudged toward observations during these same first 3 h.

Multiple cycles were completed for each experiment. The 0-h forecast (i.e., the beginning of the forecast period) for the first cycle in each experiment is 18 UTC. However, the model start time of the first cycle is either 15, 17, or 18 UTC depending on the pre-forecast length for that experiment (Table 1). Each cycle of each experiment ends at 00 UTC, which means that each experiment has a 6-h forecast for the first cycle.

The beginning of the forecast for the next cycle of each experiment is at 19 UTC, and the ending of the forecast is at 00 UTC; thus, each experiment has a 5-h forecast. Each cycle used only HRRR output from HRRR integration that begins at 15 UTC. The cycles are independent, thus no data from the WRF integration in the first cycle are used in the WRF integration in the second cycle. The cycles continue until the 23 UTC cycle, which produces a 1-h forecast.

Each cycle is referred to by the beginning of the forecast period of the cycle (t_0 in Fig. 7). For example, the VLAPS3 cycle that starts at 16 UTC is referred to as VLAPS3₁₉ since the first 3 h are pre-forecast (Table 1) and thus the forecast starts at 19 UTC.

6. Preliminary Results

Currently, only a preliminary analysis of the results of these experiments has been completed. This technical report is intended primarily to describe the methods employed in this study and provide some preliminary results, with a subsequent technical report providing a more detailed analysis of the results.

6.1 Experiment Comparison at Time of Newcastle–Moore Tornado

At 2015 UTC, the Newcastle–Moore tornado was at or near its peak strength. As part of the preliminary analysis of the experiment results, we investigated differences between the experiments at this time. The observed radar composite base reflectivity at 2015 UTC (Fig. 8) shows a broken southwest–northeast oriented line of strong convection passing through central Oklahoma and southeastern Kansas. The Newcastle–Moore tornado (black “X” in the white square) is near the rear of this line. A weak, similarly oriented line of precipitation is located over southcentral Kansas. There is also scattered precipitation in western Kansas and Oklahoma, and in the portion of southeastern Colorado in the domain.

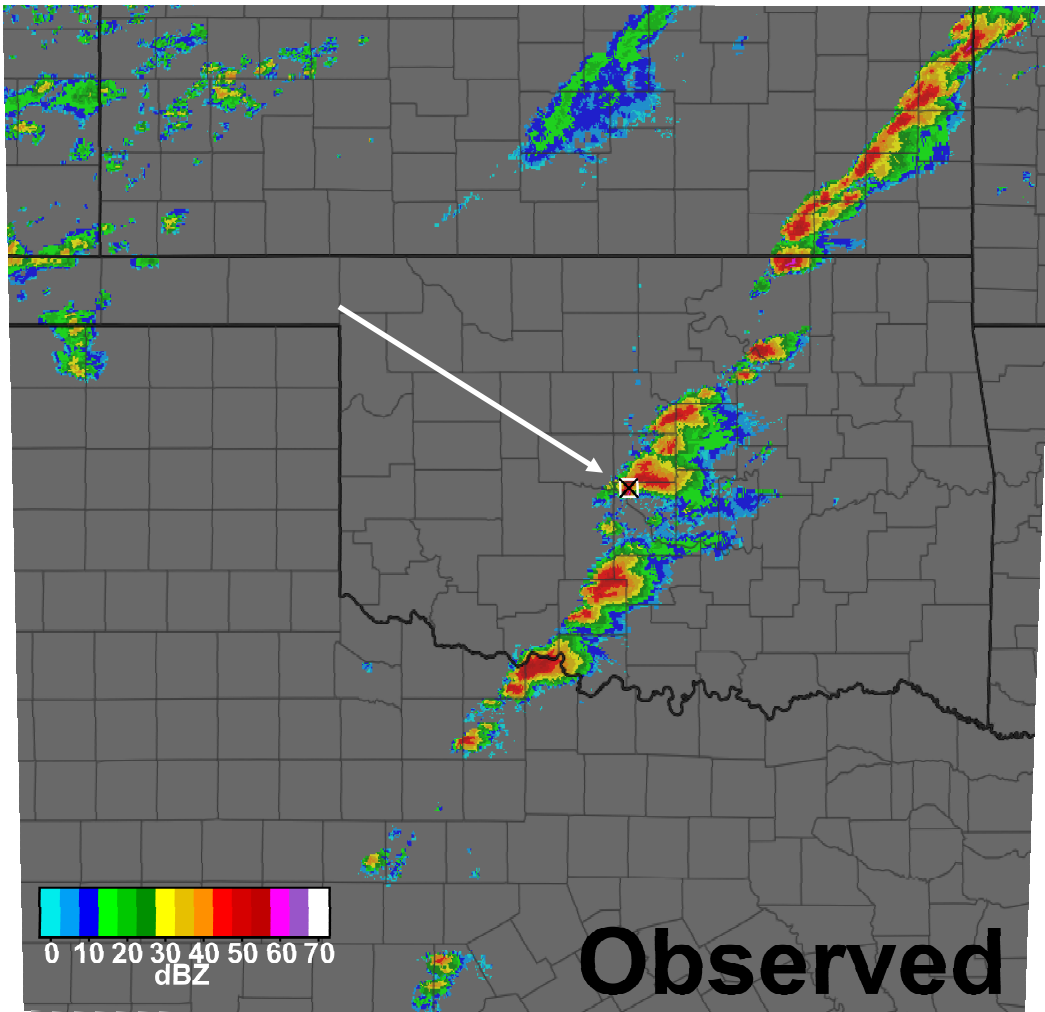


Fig. 8 Composite base reflectivity at 2015 UTC. The black X inside the white square (near the end of the white arrow) indicates the location of the Newcastle–Moore tornado at 2015 UTC. Radar reflectivity obtained from Iowa Environmental Mesonet (<http://mesonet.agron.iastate.edu/GIS/apps/rview/warnings.phtml>) and cropped to the approximate extent of the WRF-ARW model domain.

6.1.1 Comparison of Hybrid to Component Techniques

The first 4 experiments examined represent a control experiment, the 2 components of the hybrid, and the full hybrid experiment. Namely, HRRR3 is chosen as the control since it contains no data assimilation but has a 3-h pre-forecast to allow convection to spin up. VLAPS0 represents the vLAPS component of the hybrid, since it represents how vLAPS is usually applied (i.e., with no pre-forecast spin-up). OBSGRID30 represents the nudging component, with the initial conditions enhanced using an objective analysis created by Obsgrid and 3 h of observation nudging applied. VLAPS3AO is the full hybrid experiment, incorporating vLAPS as the initial conditions, analysis nudging to 15-min vLAPS analyses, and observation nudging. We first examine the results from the experiments whose 0-h

forecast is at 18 UTC (i.e., HRRR3₁₈, VLAPS0₁₈, OBSGRID3O₁₈, and VLAPS3AO₁₈).

The model-simulated lowest model level radar reflectivity of all 4 experiments at 2015 UTC (Fig. 9) generally reproduces the overall structures in the observed composite base reflectivity (Fig. 8). In particular, all 4 experiments show the main line of convection along the proper alignment, scattered precipitation in the northwestern corner of the domain, and some precipitation in the northcentral portion of the domain. However, there are significant differences in the details of predicted precipitation.

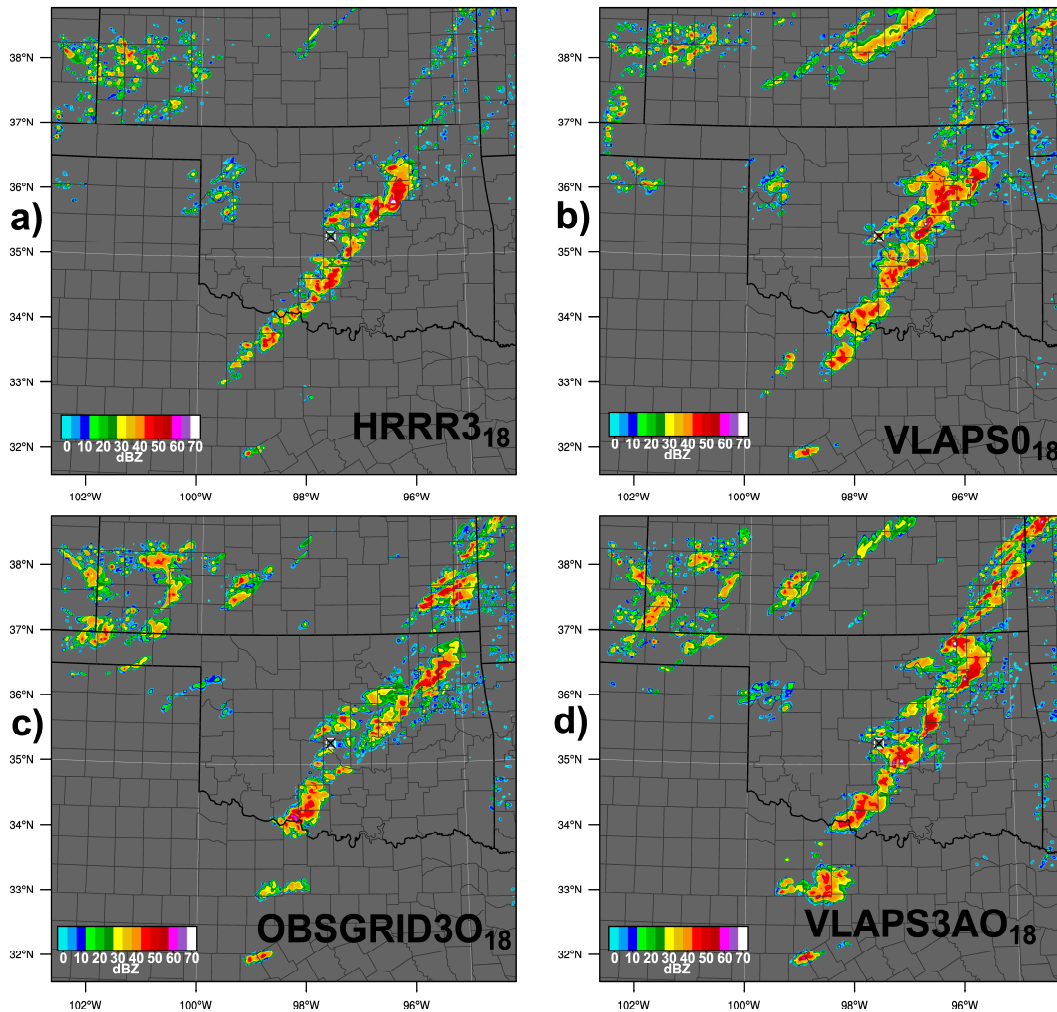


Fig. 9 WRF-ARW lowest model level radar reflectivity at 2015 UTC on 20 May 2013 for a) HRRR3₁₈, b) VLAPS0₁₈, c) OBSGRID3O₁₈, and d) VLAPS3AO₁₈. The location of the Newcastle–Moore tornado at 2015 UTC is indicated by the black “X” within the white square (in the same location as marked by the arrow in Fig. 8).

There is considerable variation among the experiments in the prediction of the area of light precipitation observed over southcentral Kansas (Fig. 8; top center of plot). HRRR3₁₈ (Fig. 9a) and even more so OBSGRID3O₁₈ (Fig. 9c) underpredict the coverage of this feature. VLAPS0₁₈ (Fig. 9b) predicts 2 roughly parallel lines of convection, with the leading line much stronger than the observed structure, and the trailing line more scattered than observed. While VLAPS3AO₁₈ (Fig. 9d) predicts higher reflectivity than observed and with less coverage than observed, it appears to best predict the coverage of this precipitation.

The portion of the main convective line over southeastern Kansas (Fig. 8) shows substantial differences between the experiments. HRRR3₁₈ (Fig. 9a) and VLAPS0₁₈ (Fig. 9b) predict convection that is much more scattered than the continuous line observed, although VLAPS0₁₈ appears to perform better than HRRR3₁₈ as it indicates greater coverage than HRRR3₁₈. OBSGRID3O₁₈ (Fig. 9c) predicts stronger convection with much more coverage than HRRR3₁₈ and VLAPS0₁₈ but does not simulate the linear nature of the convection as well as VLAPS3AO₁₈ (Fig. 9d).

Over Oklahoma, the predictions of the main convective line also differ among the experiments. Convection extends too far into the northeastern corner of Oklahoma in OBSGRID3O₁₈ (compare Fig. 9c to Fig. 8) and VLAPS3AO₁₈ (Fig. 9d). HRRR3₁₈ (Fig. 9a) and VLAPS0₁₈ (Fig. 9b) do not seem to have this issue. Also, VLAPS3AO₁₈ also appears to better represent the discrete nature of the convection in the main convective line than the other experiment.

All 4 experiments indicate moist convective elements on the western edge of Oklahoma, but radar indicates that this area was free of precipitation at this time (Fig. 8). In this case, OBSGRID3O₁₈ (Fig. 9c) predicts weaker convection and with less coverage than any of the other experiments, while VLAPS3AO₁₈ (Fig. 9d) appears to predict less coverage of stronger convection (>30 dBZ) than the other 2 experiments (HRRR3₁₈ and VLAPS0₁₈).

While all 4 experiments predict a relatively small area of convection in the far south of the central portion of the domain (Fig. 9) consistent with observations (Fig. 8), some predict convection a couple counties north of this location, which is inconsistent with observed radar. VLAPS3AO₁₈ (Fig. 9d) predicts this convection to be the most widespread while OBSGRID3O₁₈ (Fig. 9c) also predicts this area of convection but forecast that it would not be as strong as indicated by VLAPS3AO₁₈.

These 4 experiments vary in the predictions near the observed location of the Newcastle–Moore tornado at 2015 UTC. OBSGRID3O₁₈ (Fig. 9c) shows convection just northwest of this location while HRRR3₁₈ (Fig. 9a) and

VLAPS3AO₁₈ (Fig. 9d) show convection north of this location. VLAPS0₁₈ (Fig. 9b) indicate convection north of this location. VLAPS0₁₈ (Fig. 9b) is the only experiment that predicts convection at the location of the Newcastle–Moore tornado at this time.

6.1.2 Comparison between Varieties of Component Techniques

While the previous section explored the difference between the full hybrid versus its components, here we investigate differences between varieties of the component techniques that differ in the length of the pre-forecast or on what types of nudging are applied. In this section, we again solely examine the cycle with an 18 UTC 0-h forecast. First, we compare HRRR0₁₈ versus HRRR3₁₈, then VLAPS0₁₈ versus VLAPS1₁₈ and VLAPS3₁₈, and finally VLAPS3AO₁₈ versus VLAPS3A₁₈ and VLAPS3O₁₈.

Comparing the 2 experiments that use neither vLAPS analyses nor nudging (HRRR0₁₈ and HRRR3₁₈) reveals the potential benefit of a 3-h period for the model spin-up. The experiments only differ in that HRRR0₁₈ starts at 18 UTC, whereas HRRR3₁₈ starts at 15 UTC and thus contains 3 h (15–18 UTC) during which model spin-up can occur. The lowest model level model-simulated reflectivity in HRRR0₁₈ (Fig. 10b) is very similar to HRRR3₁₈ (Fig. 10a) at 2015 UTC. Without the 3-h spin-up, HRRR0₁₈ still reproduces the same overall structure of precipitation as HRRR3₁₈. However, for the time under evaluation (2015 UTC), even though HRRR0₁₈ does not have the 15–18 UTC time for spin-up, it has had just over 2 h to spin up the convection. HRRR0₁₈ increases the coverage of the precipitation halfway across the northern edge of the domain that HRRR3₁₈ underpredicted but shows the precipitation as more intense than radar indicated (Fig. 10c) and does not extend the convection nearly far enough to the southwest. Contrary to observations and HRRR3₁₈, HRRR0₁₈ produces scattered convection between this element (the precipitation halfway across the northern edge of the domain) and the widespread scattered convection in the northwest corner of the domain. Both experiments fail to reproduce the line of convection across southeastern Kansas. In the area of the Newcastle–Moore tornado, moist convection is somewhat farther away to the north but much closer to the south in HRRR0₁₈ as compared to HRRR3₁₈. Overall, it is not clear whether HRRR0₁₈ or HRRR3₁₈ performs better at this time. The similarities between HRRR0₁₈ and HRRR3₁₈ are not entirely unexpected since both are initialized using output from the same 3-km HRRR simulation and since both experiments are using physics options very similar to those used in the HRRR simulation.

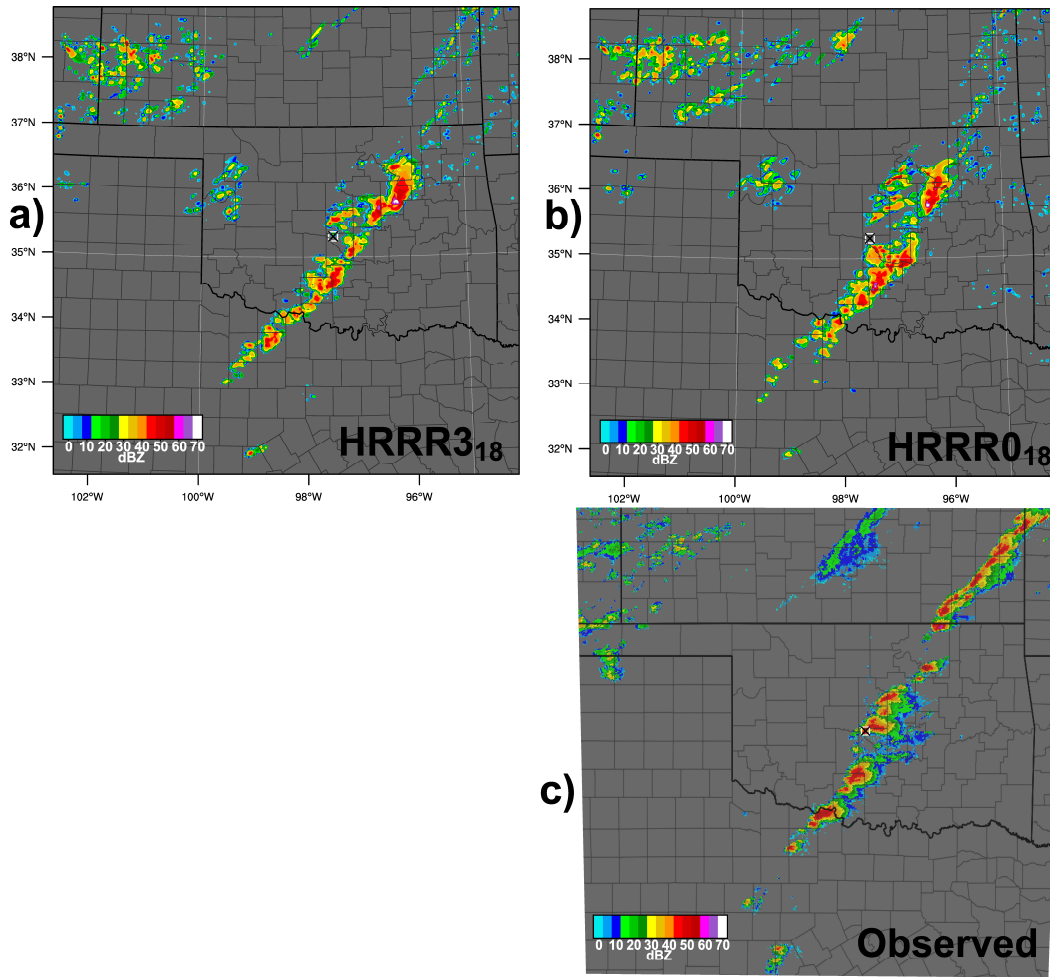


Fig. 10 WRF-ARW lowest model level radar reflectivity at 2015 UTC on 20 May 2013 for a) HRRR3₁₈, b) HRRR0₁₈, and c) observed base reflectivity composite. The location of the Newcastle–Moore tornado at 2015 UTC is indicated by the black “X” within the white square.

The experiments VLAPS0₁₈, VLAPS1₁₈, and VLAPS3₁₈ assist in evaluating whether using a more recent vLAPS analysis for initial conditions overwhelms whatever benefits are accrued via additional model spin-up time. At the 2015 UTC time shown, experiments VLAPS0₁₈, VLAPS1₁₈, and VLAPS3₁₈ have integrated 2.25, 3.25, and 5.25 h, respectively, after accounting for the varying pre-forecast times assigned (0, 1, and 3 h) and the 2.25 h between the 1800 UTC start of this cycle and the 2015 UTC time being discussed. The weak line of precipitation in central Kansas (extending toward the southwest from the north-central edge of the observed radar; Fig. 11d) was overpredicted in VLAPS0₁₈ (Fig. 11a), while adding an hour pre-forecast (VLAPS1₁₈; Fig. 11b) significantly weakened this precipitation, an additional 2 h of pre-forecast (VLAPS3₁₈; Fig. 11c) results in a structure that better resembles that observed. The line of convection in southeastern Kansas becomes better organized with increased pre-

forecast time and more closely matches the line observed. The southern end of the main line of convection varies among the experiments, but it is difficult to determine which performs best. The spatial extent of the spurious convection in the northwestern portion of Oklahoma appears to be minimized with a 3-h pre-forecast, although a 0-h pre-forecast outperforms a 1-h pre-forecast. Overall, it appears that the 3-h pre-forecast experiment performs best in terms of simulated reflectivity at 2015 UTC for the 18 UTC cycle. This suggests the potential importance of allowing at least some additional model spin-up time following a vLAPS “hot start” analysis.

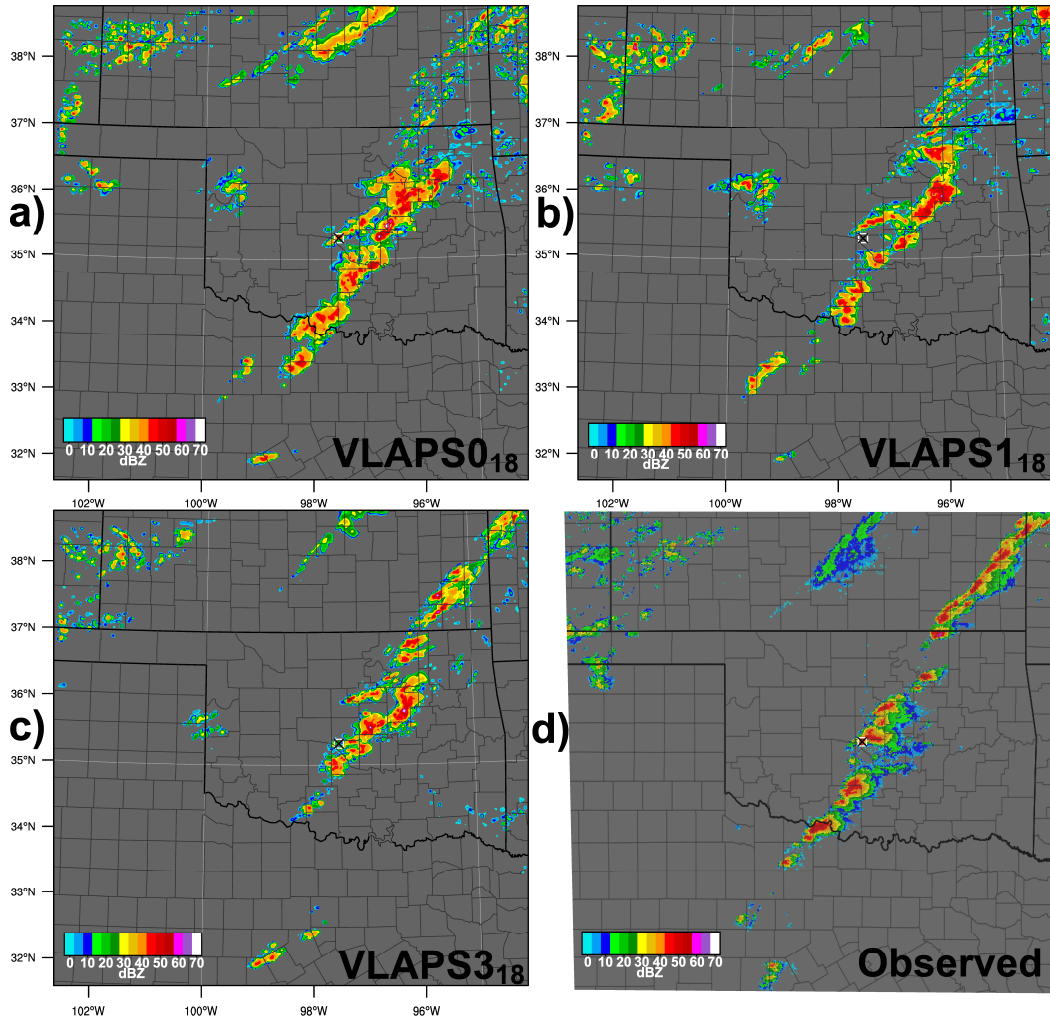


Fig. 11 WRF-ARW lowest model level radar reflectivity at 2015 UTC on 20 May 2013 for a) VLAPS0₁₈, b) VLAPS1₁₈, c) VLAPS3₁₈, and d) observed base reflectivity composite. The location of the Newcastle–Moore tornado at 2015 UTC is indicated by the black “X” within the white square.

The next comparison evaluates the relative contributions of the analysis nudging versus the observation nudging in the hybrid data assimilation using 3

experiments that all are initialized with the vLAPS analysis and include a 3-h pre-forecast time period with data assimilation. In addition to being initialized with the vLAPS analysis, VLAPS3A₁₈ also analysis nudges toward 15-min vLAPS analyses during the 3-h pre-forecast. VLAPS3O₁₈ does not perform analysis nudging but includes 3 h of observation nudging, while the full hybrid experiment VLAPS3AO₁₈ performs both. The full hybrid experiment (VLAPS3AO₁₈; Fig. 12a) seems to best reproduce the northern portion of the main line of convection (north of Oklahoma), while it and the other analysis-nudging experiment (VLAPS3A₁₈; Fig. 12b) both seem to best reproduce the linear structure across central Kansas (top-center of plots) compared to the nonanalysis-nudging experiment (VLAPS3O₁₈; Fig. 12c). However, the nonanalysis nudging experiment (VLAPS3O₁₈; Fig. 12c) best minimizes the erroneously predicted precipitation in the western edge of Oklahoma. Just south of the southern end of the main convective line, VLAPS3AO₁₈ produces a convective element not observed (Fig. 12d). While VLAPS3A₁₈ (Fig. 12b) and VLAPS3O₁₈ (Fig. 12c) do not predict an area of convection as large as that predicted by VLAPS3AO₁₈, they both appear to produce smaller convective cells that appear to be erroneous.

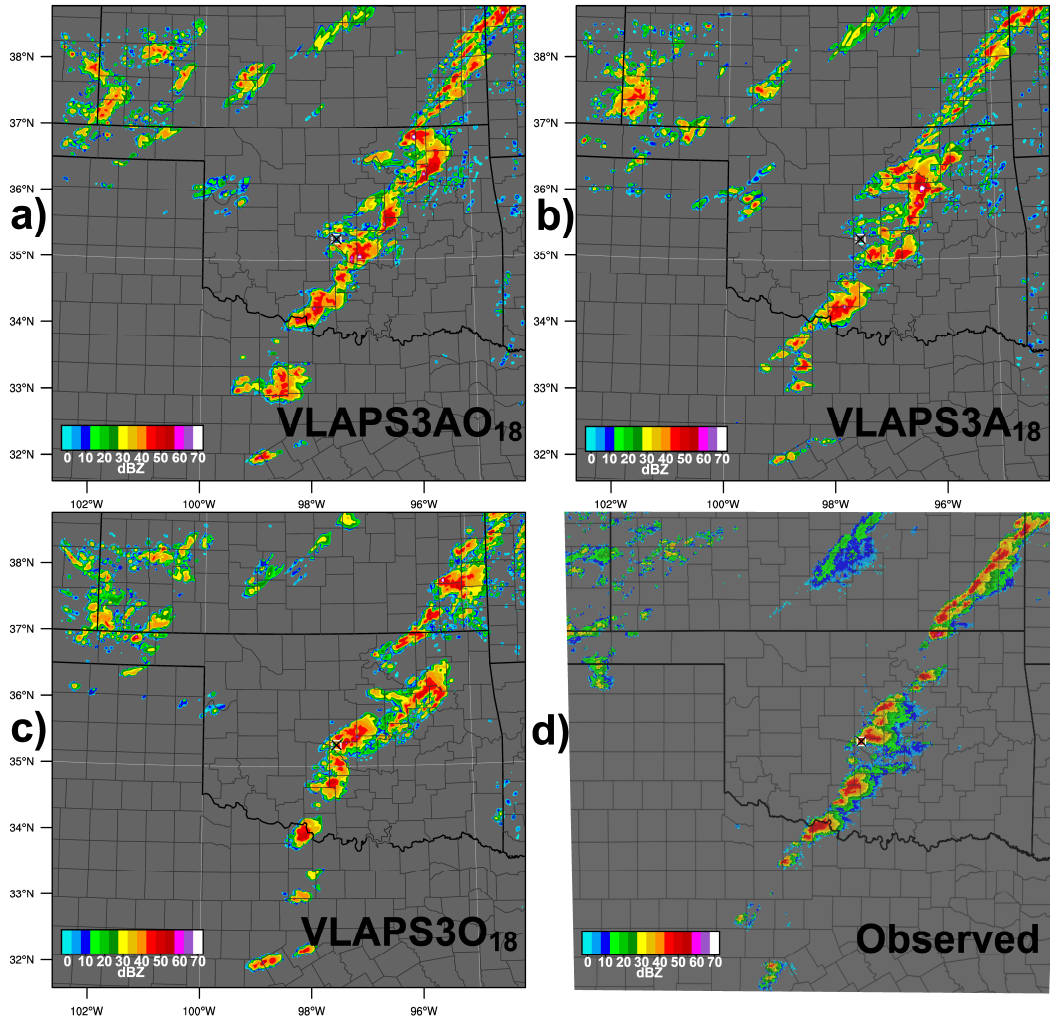


Fig. 12 WRF-ARW lowest model level radar reflectivity at 2015 UTC on 20 May 2013 for a) VLAPS3AO₁₈, b) VLAPS3A₁₈, c) VLAPS3O₁₈, and d) observed base reflectivity composite. The location of the Newcastle–Moore tornado at 2015 UTC is indicated by the black “X” within the white square.

In the region near Moore, VLAPS3AO₁₈ (Fig. 12a) and VLAPS3A₁₈ (Fig. 12b) indicate strong convection to the southeast (stronger in VLAPS3AO₁₈), but only weaker returns in the immediate vicinity of Moore (also stronger in VLAPS3AO₁₈). VLAPS3O₁₈ differs in that it indicates convection either over or very close to Moore. Although there are differences between the vLAPS experiments with nudging, it is not clear which experiment performs best overall at 2015 UTC.

6.1.3 Comparison of Different Cycles

Generally, one might expect that forecasts initialized closer in time to an event would perform better than forecasts initialized farther in the past, with the caveat that sufficient time must be available between the model start and the event for the

model to spin-up. This is because the longer the model integrates without the benefit of observations to constrain the solution to reality, the longer errors introduced by the initial conditions have to grow, and the longer conditions influenced by the lateral boundary conditions have to advect to the area of interest. Therefore, more precisely, assuming sufficient model spin-up time has already occurred, one would expect that over short-term forecasts the longer the model integrates without being constrained by observations, the larger the errors in the solution.

The 2015 UTC model-simulated radar reflectivity from 3 HRRR3 cycles are compared to the observed radar reflectivity in Fig. 13. Figure 13a shows HRRR3₁₈ after 3-h of model spin-up (15–18 UTC) and 2.25 h of subsequent model integration, Fig. 13b shows HRRR3₁₉ after 3 h of model spin-up (16–19 UTC) and 1.25 h of subsequent model integration, and Fig. 12c shows HRRR3₂₀ after 3 h of model spin-up (17–20 UTC) and 0.25 h of subsequent model integration. For HRRR3 these 3 cycles generally show fairly similar solutions at 2015 UTC. All 3 simulations show the main line of observed convection (Fig. 13d), although much too weak in Kansas, scattered convection in the northwestern corner of the domain, a too-weak short line in the northcentral portion of the domain, and all inaccurately place convection in western Oklahoma. None of the cycles place strong convection over Moore at this time. It is important to note that HRRR3 does not do any assimilation and that all of the cycles of HRRR3 are driven by output from the same HRRR model forecast. Therefore, the HRRR3 cycle that integrates the shortest before the 2015 UTC time examined here (HRRR3₂₀) does not include any newer observations than the HRRR3 cycle that integrates longest before 2015 UTC (HRRR3₁₈). Thus, it is not surprising that more recent cycles do not appear to improve the forecast at 2015 UTC. HRRR3 does serve an important purpose in the comparison here in that it provides context for evaluating other experiments since HRRR3 indicates that change in the solution at 2015 UTC is caused solely by initializing using HRRR at different times.

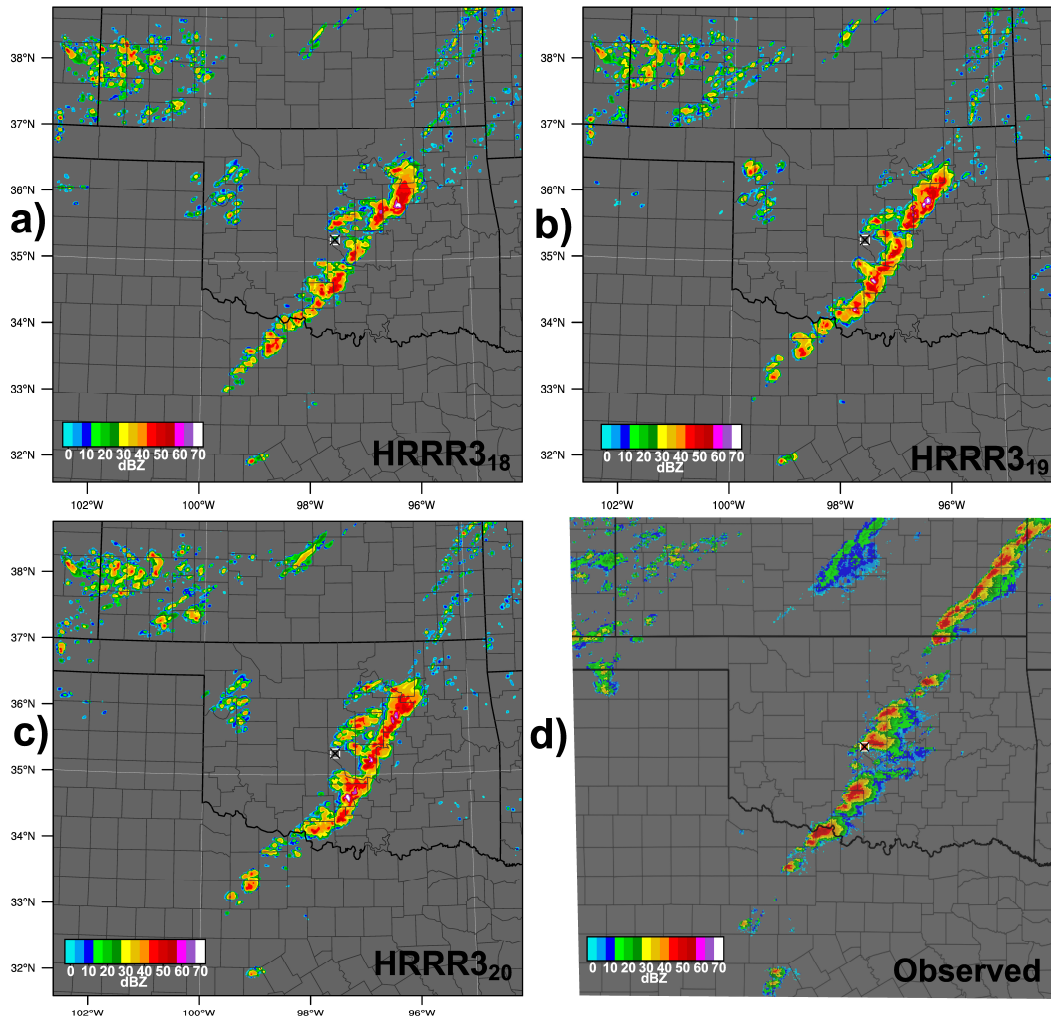


Fig. 13 WRF-ARW lowest model level radar reflectivity at 2015 UTC on 20 May 2013 for a) HRRR3₁₈, b) HRRR3₁₉, c) HRRR3₂₀, and d) observed base reflectivity composite. The location of the Newcastle–Moore tornado at 2015 UTC is indicated by the black “X” within the white square.

Unlike the HRRR3 simulations, in VLAPS3 later cycles include newer observations and thus hopefully provide better forecasts. The 2015 UTC forecast in Fig. 14a for VLAPS3₁₈ is based on a WRF simulation started at 15 UTC with a vLAPS analysis, integrated 3 h (15–18 UTC) to allow the model solution to spin up, and then integrated another 2.25 h to 2015 UTC. VLAPS3₁₉ (Fig. 14b) starts 1 h later, thus the initial conditions include observations that are 1 h more recent than VLAPS3₁₈, and similarly VLAPS3₂₀ (Fig. 14c) includes observations 2 h more recent than VLAPS3₁₈.

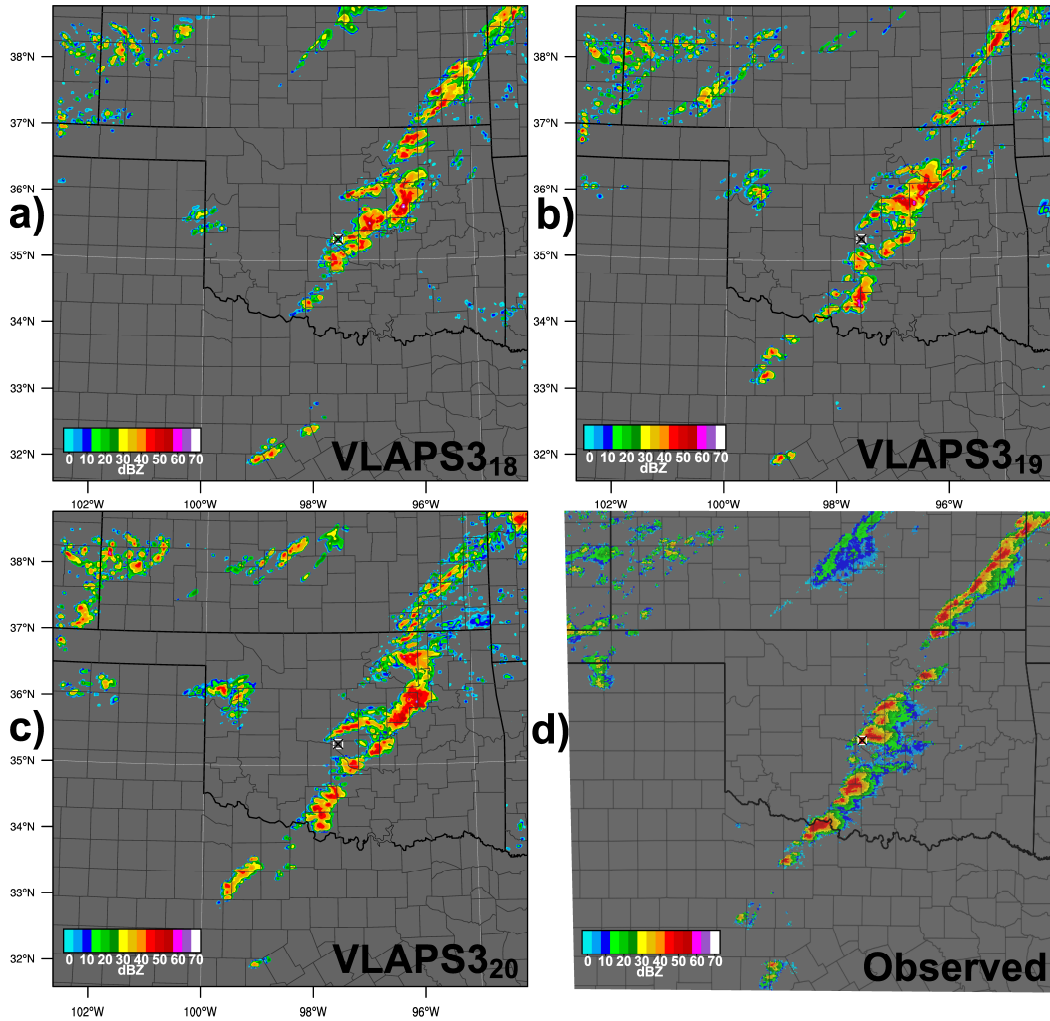


Fig. 14 WRF-ARW lowest model level radar reflectivity at 2015 UTC on 20 May 2013 for a) VLAPS3₁₈, b) VLAPS3₁₉, c) VLAPS3₂₀, and d) observed base reflectivity composite. The location of the Newcastle–Moore tornado at 2015 UTC is indicated by the black “X” within the white square.

Clear variations are seen among the 3 cycles of VLAPS3 discussed here. The location of the weak line of precipitation in the northcentral portion of the domain (central Kansas) is predicted well in VLAPS3₁₈ (Fig. 14a), while the coverage is lacking and the intensity is larger than observed (Fig. 14d). However, starting with 1-h newer vLAPS analyses (16 UTC analysis in VLAPS3₁₉; Fig. 14b) nearly removes this line and results in scattered precipitation just west of this, both contrary to observations. Moving forward to using the 17 UTC vLAPS analysis (VLAPS3₂₀; Fig. 14c) allows this line to be re-established but results in a series of parallel lines of precipitation. In terms of this line of precipitation initializing WRF with an earlier vLAPS analysis (15 UTC) and allowing WRF a longer spin-up time results in the forecast that best matches the observed nature of this precipitation. The northeastern portion of the main line of convection least

resembles the continuous line of precipitation observed in the experiment using the newest vLAPS analysis (VLAPS3₂₀; Fig. 14c). The erroneous area of precipitation in westernmost Oklahoma appears to be strongest in the cycle using the newest vLAPS analysis (VLAPS3₂₀; Fig. 14c). In terms of the location of the Newcastle–Moore tornado, all 3 experiments indicate this location is on the backside of the line of convection, which is also indicated by radar. VLAPS3₁₈ indicates precipitation at this location, while VLAPS3₁₉ and VLAPS3₂₀ show a line of convection stretching southwest from the main line of convection to just north of this location (closer to Newcastle–Moore in VLAPS3₂₀ than in VLAPS3₁₉). Radar (Fig. 14d) indicates a convective element aligned generally west-east, with the Newcastle–Moore tornado near the western edge of this element. Thus, there are some similarities between the VLAPS3 and radar-observed representations of the convection in the region of the Newcastle–Moore tornado.

Both VLAPS0 and VLAPS3 are initialized with vLAPS analyses, but VLAPS0 assigns the 0-h forecast time to the model start time, while VLAPS3 assigns the 0-h forecast time 3 h after the model start time to allow time for model spin-up. Thus, the VLAPS3₂₀ forecast at 2015 UTC (Fig. 14c) is initialized with a vLAPS analysis at 17 UTC and integrated 3.25 h, while the VLAPS0₁₈ forecast at 2015 UTC (Fig. 15a) is initialized with a vLAPS analysis at 18 UTC and integrated 2.25 h. Therefore, Figs. 14 and 15 provide the 2015 UTC forecast by WRF simulations initialized with vLAPS analysis at 15 (Fig. 14a), 16 (Fig. 14b), 17 (Fig. 14c), 18 (Fig. 15a), 19 (Fig. 15b), and 20 UTC (Fig. 15c).

Encouragingly, the VLAPS0₂₀ 2015 UTC forecast (Fig. 15c) relatively closely matches the radar's observation at this time (Fig. 15d). Since the vLAPS analyses used to initialize the VLAPS0 experiments incorporate radar observations, one would expect the very short-term model forecast to closely resemble the radar observations if the vLAPS analysis is sufficiently in balance with the model's dynamics and physics. If the vLAPS analysis were substantially out of balance with the WRF model's dynamics and physics, the WRF model solution might quickly diverge from observations as large adjustments occur to bring the solution in balance with the model's equations. Thus, the similarity here between model and radar suggests that the vLAPS analyses may be in fairly good balance with WRF physics and dynamics. However, significant further analysis would be necessary to fully address this issue.

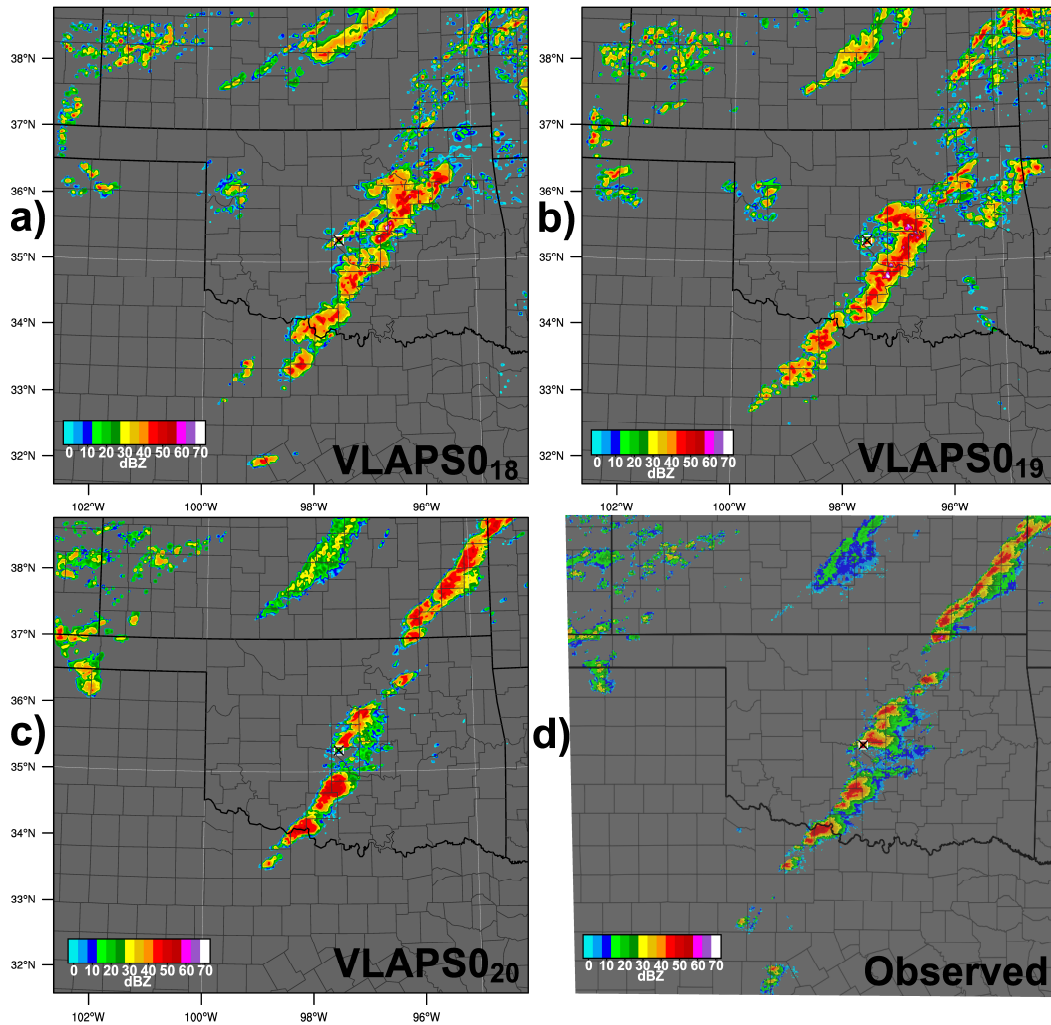


Fig. 15 WRF-ARW lowest model level radar reflectivity at 2015 UTC on 20 May 2013 for a) VLAPS018, b) VLAPS019, c) VLAPS020, and d) observed base reflectivity composite. The location of the Newcastle–Moore tornado at 2015 UTC is indicated by the black “X” within the white square.

As the analysis time approaches the forecast time, the secondary line of convection, the one in the northcentral portion of the domain, is better predicted. However, it appears to be overpredicted even in VLAPS020 (Fig. 15c). The northeast portion of the main line of convection is not well simulated in either VLAPS018 (Fig. 15a) or VLAPS019 (Fig. 15b), but VLAPS020 does much better. The west-to-east oriented convection that spawned the Newcastle–Moore tornado is not well-simulated in any of the cycles, even in VLAPS020. The erroneous area of convection in far western Oklahoma is predicted in both VLAPS018 and VLAPS019, but is omitted in VLAPS020; however, it may be that VLAPS020 has not had sufficient time to spin up this convection and thus will predict this convection delayed from the other simulations. Contrary to the improvement seen with decreasing lead time in most convective elements, the southernmost observed

convective element is predicted by VLAPS0₁₈, but not by VLAPS0₁₉ or VLAPS0₂₀. Overall, the experiment with the most recent vLAPS analysis appears to perform best (VLAPS0₂₀), but since the model has only had 15 min of integration, it is unclear whether this benefit persists past the beginning of the model forecast.

Because of differences in the data assimilation techniques used by OBSGRID3O and VLAPS3/VLAPS0, care must be taken in interpreting comparisons between OBSGRID3O and VLAPS3/VLAPS0. OBSGRID3O has the advantage over VLAPS3 in that in addition to incorporating observations into its initial conditions (via the objective analysis produced by Obsgrid) it also assimilates observations through the first 3 h of the model integration. Thus, the newest observations assimilated into OBSGRID3O₁₈ are at 18 UTC while the newest observations assimilated into VLAPS3₁₈ are at 15 UTC. While VLAPS0₁₈ is more comparable to OBSGRID3O₁₈ in that both may be using 18 UTC observations, OBSGRID3O₁₈ has the advantage of 3 h of model spin-up and application of observations to the model solution over 3 h rather than at only the initial time. Because of these reasons, one must be careful not to conclude that Obsgrid analyses are better than vLAPS analysis solely due to comparisons between Obsgrid-initialized and vLAPS-initialized experiments that started at the same time (e.g., OBSGRID3O₁₈ and VLAPS3₁₈). Ultimately, it is the combination of vLAPS analyses and the nudging technique that we hypothesize will create the best forecast.

The OBSGRID3O solution varies among the model start times shown in Fig. 16 (15 UTC in Fig. 16a, 16 UTC in Fig. 16b, and 17 UTC in Fig. 16c). The modeled convection in southeastern Kansas evolves closer to the observed linear structure (Fig. 16d) at later forecast start times, while the modeled convection just south in northeastern Oklahoma strengthens contrary to the observed gap in the line here. Encouragingly, the convection just north of Moore strengthens considerably with shorter lead times, so that in OBSGRID3O₂₀, greater than 70 dBZ is simulated north of Moore (Fig. 16c). Although the strongest modeled convection is somewhat north of the observed storm, this solution is much closer to the observed radar reflectivity than earlier cycles. By the OBSGRID3O₂₀ cycle (Fig. 16c), a broken line of precipitation in central Kansas forms near the axis of the observed line in this region (Fig. 16d), but the modeled line is not as continuous and not as wide as the observations. In addition, behind this line OBSGRID3O₂₀ erroneously shows a strong line of convection stretching into far northern Texas. OBSGRID3O₁₉ and OBSGRID3O₂₀ also show stronger convection in the southern quarter of the domain than observed. Also, the erroneous area of convection in western Oklahoma simulated in many of the

experiments becomes much more prominent with shorter lead time. In general, OBSGRID3O appears to simulate overly strong convection at cycles with shorter lead times (e.g., OBSGRID3O₂₀) but better simulates the convection in southeastern Kansas and in the Moore, Oklahoma, region.

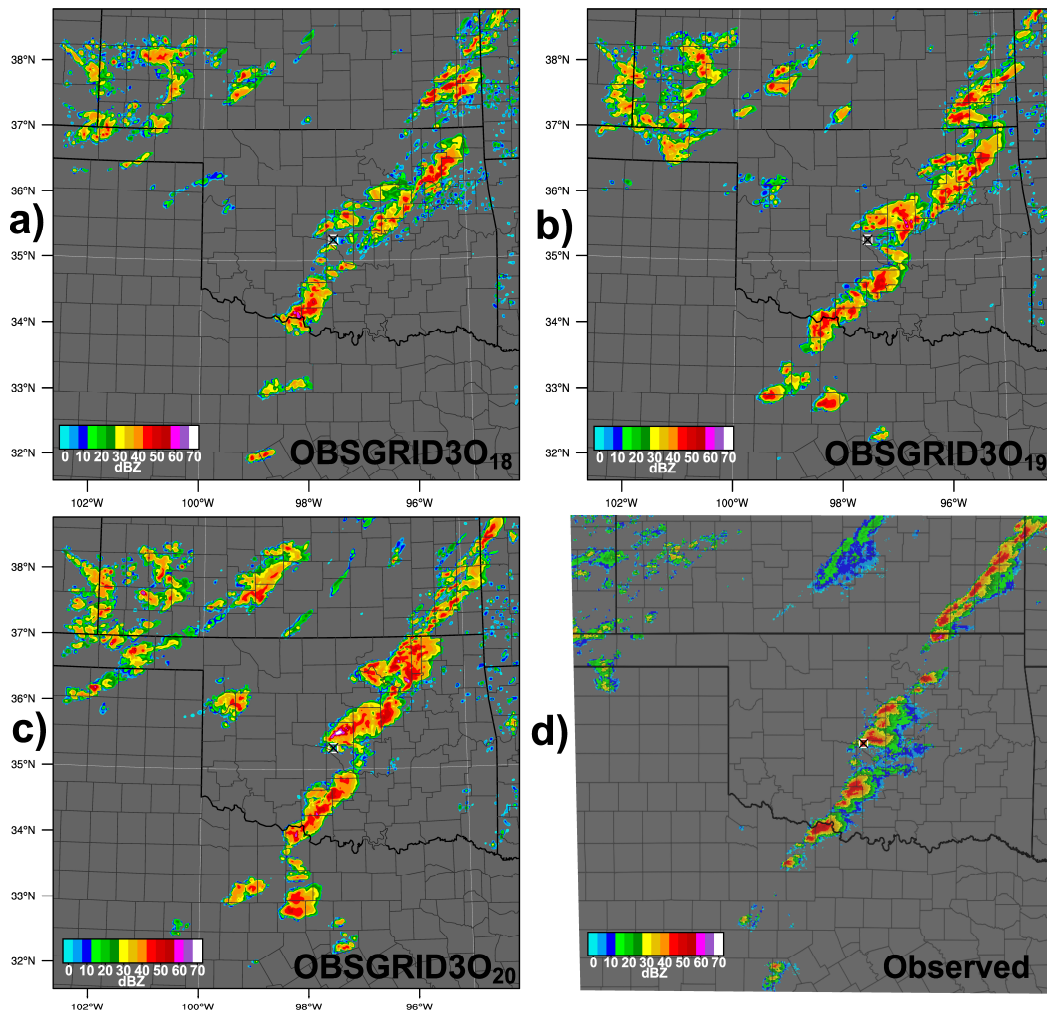


Fig. 16 WRF-ARW lowest model level radar reflectivity at 2015 UTC on 20 May 2013 for a) OBSGRID3O₁₈, b) OBSGRID3O₁₉, c) OBSGRID3O₂₀, and d) observed base reflectivity composite. The location of the Newcastle–Moore tornado at 2015 UTC is indicated by the black “X” within the white square.

The full hybrid experiment (VLAPS3AO) includes both the vLAPS analysis in initial conditions as used by VLAPS3, the observation nudging used in OBSGRID3O and VLAPS3O, and the analysis nudging toward vLAPS analyses during the first 3 h used in VLAPS3A. VLAPS3AO simulates the northeastern part of the main line of convection (in southeastern Kansas) for VLAPS3AO₁₈ (Fig. 17a), VLAPS3AO₁₉ (Fig. 17b), and VLAPS3AO₂₀ (Fig. 17c), albeit with more scattered convection along the axis of the line than observed. VLAPS3AO₁₉ and VLAPS3AO₂₀ forecast less convection in the portion of the main convective

line in far northern Oklahoma than VLAPS3AO₁₈ and more consistent with the gap seen in the line in the 2015 UTC radar reflectivity. Overprediction of convection in the southern quarter of the domain in VLAPS3AO₁₈ and VLAPS3AO₁₉ is improved in VLAPS3AO₂₀. Overall, the VLAPS3AO₁₉ cycle in particular overpredicts the coverage of convection. While VLAPS3AO₁₈ predicts west-to-east convection just north of the Newcastle–Moore tornado, VLAPS3AO₁₉ and VLAPS3AO₂₀ both predict strong convection (~70 dBZ) just north of the tornado as part of a southwest-northeast oriented element. These cycles in the experiment using vLAPS analysis for initial conditions without any nudging (VLAPS3₁₉, Fig. 14b; VLAPS3₂₀, Fig. 14c) did not produce convection close to the Newcastle–Moore tornado as strong as that in VLAPS3AO.

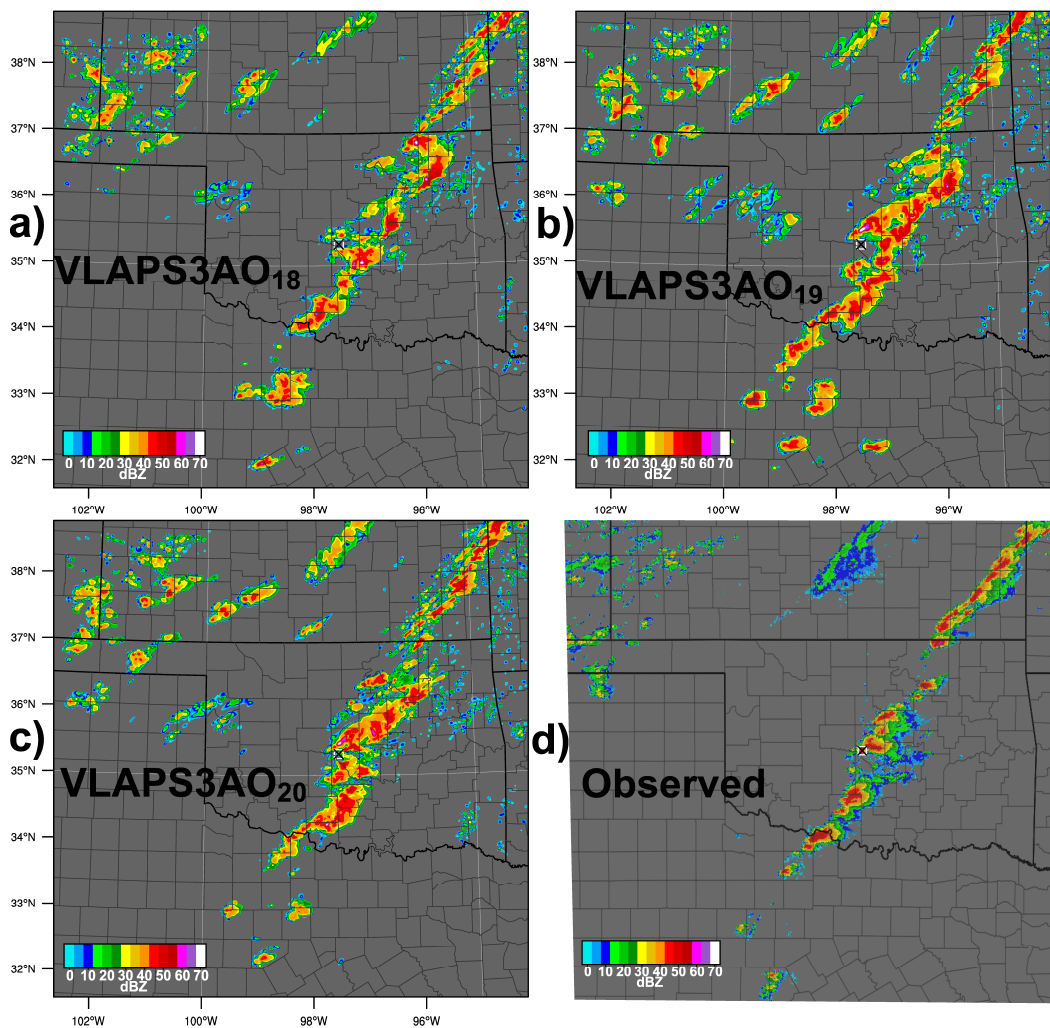


Fig. 17 WRF-ARW lowest model level radar reflectivity at 2015 UTC on 20 May 2013 for a) VLAPS3AO₁₈, b) VLAPS3AO₁₉, c) VLAPS3AO₂₀, and d) observed base reflectivity composite. The location of the Newcastle–Moore tornado at 2015 UTC is indicated by the black “X” within the white square.

6.2 Ability of Hybrid to Simulate Strong Moist Convection

While the previous section focused on comparing different experiments and cycles, here we demonstrate the capability of the full hybrid experiment (VLAPS3AO) to simulate strong convection. The goal here is not to demonstrate that VLAPS3AO simulates the supercell that spawned the Newcastle–Moore tornado consistently with observations, but rather to show that while using the full hybrid data assimilation technique, the model can simulate a strong storm with features consistent with those expected in strong moist convection.

The model-simulated radar reflectivity at the lowest model level is shown for VLAPS3AO₁₈ at 2015 UTC in Fig. 18 along with the model-simulated wind at the lowest prognostic level (≈ 13 m AGL). Ahead of the main line of convection, winds are from the south while behind the line, there is a lot of variation in the wind directions. In order for the wind barbs to be legible, only winds from a small portion of the model grid points are plotted (the model has 800 grid points in each direction). We focus on a storm southeast of the actual location of the Newcastle–Moore tornado (small white square with black X)—namely, looking at the area covered by the white box with horizontal plots and at the west–east line (or portions thereof) with cross sections. The zoomed-in view of the lowest model level reflectivity and winds (Fig. 19) shows a core of approximately 70 dBZ reflectivity within a much larger area of 40+ dBZ reflectivity. A much more detailed view of the surface winds is available in this zoomed-in image (Fig. 19) compared to the whole domain view (Fig. 18). Here, south winds are seen at the surface outside of the storm (southeast corner), with winds flowing strongly away from the area with highest reflectivity except on its western side (the wind barbs indicate winds of $25+ \text{ ms}^{-1}$ on the east side of this area). An area with slightly lower model-simulated reflectivities (peaking in the mid-60s dBZ) is predicted just west of the area with maximum reflectivities.

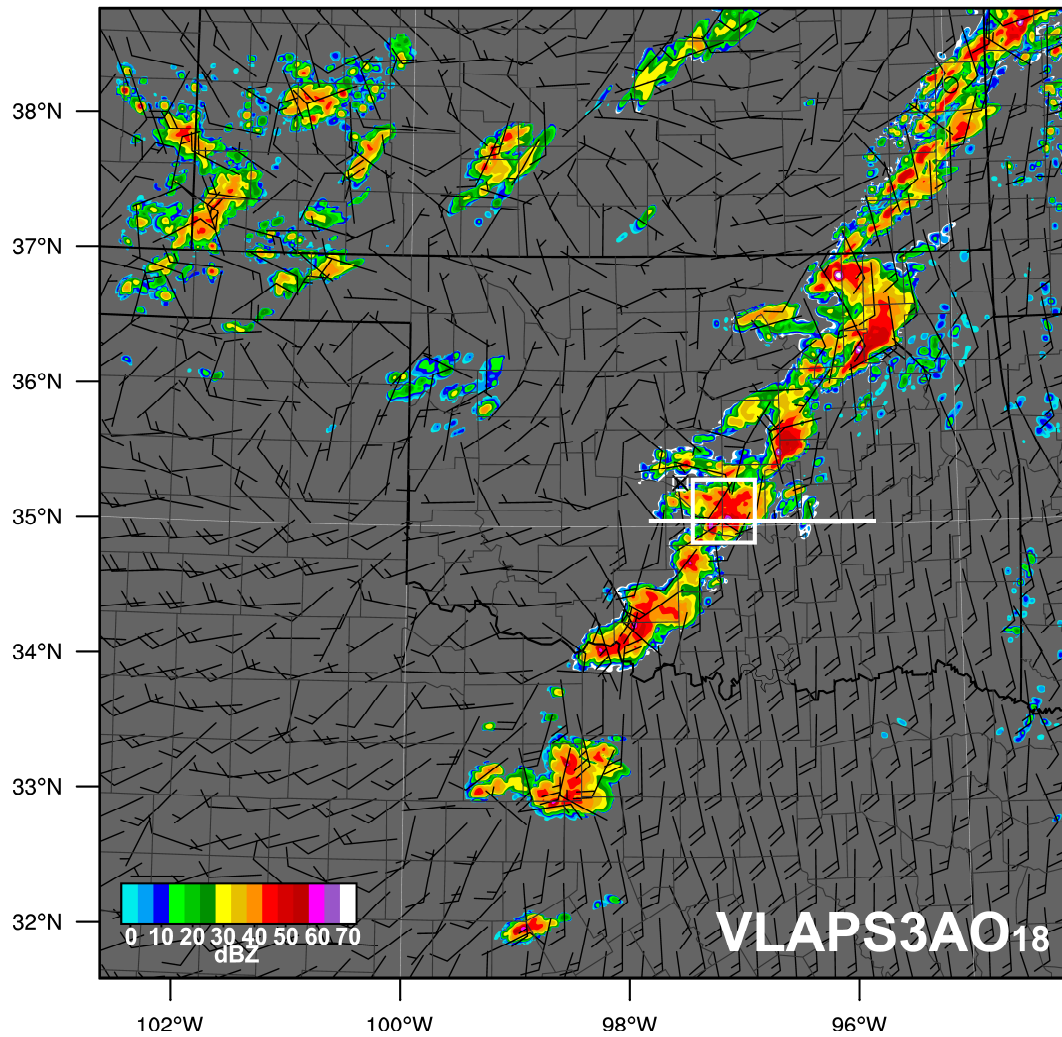


Fig. 18 WRF-ARW lowest model level radar reflectivity at 2015 UTC on 20 May 2013 for VLAPS3AO₁₈. The location of the Newcastle–Moore tornado at 2015 UTC is indicated by the black “X” within the small white square. The large white square indicates the area shown in Fig. 19, and the white horizontal line indicates the location of the cross section shown in Fig. 20. Each half barb is 2.5 ms^{-1} and each full barb is 5.0 ms^{-1} .

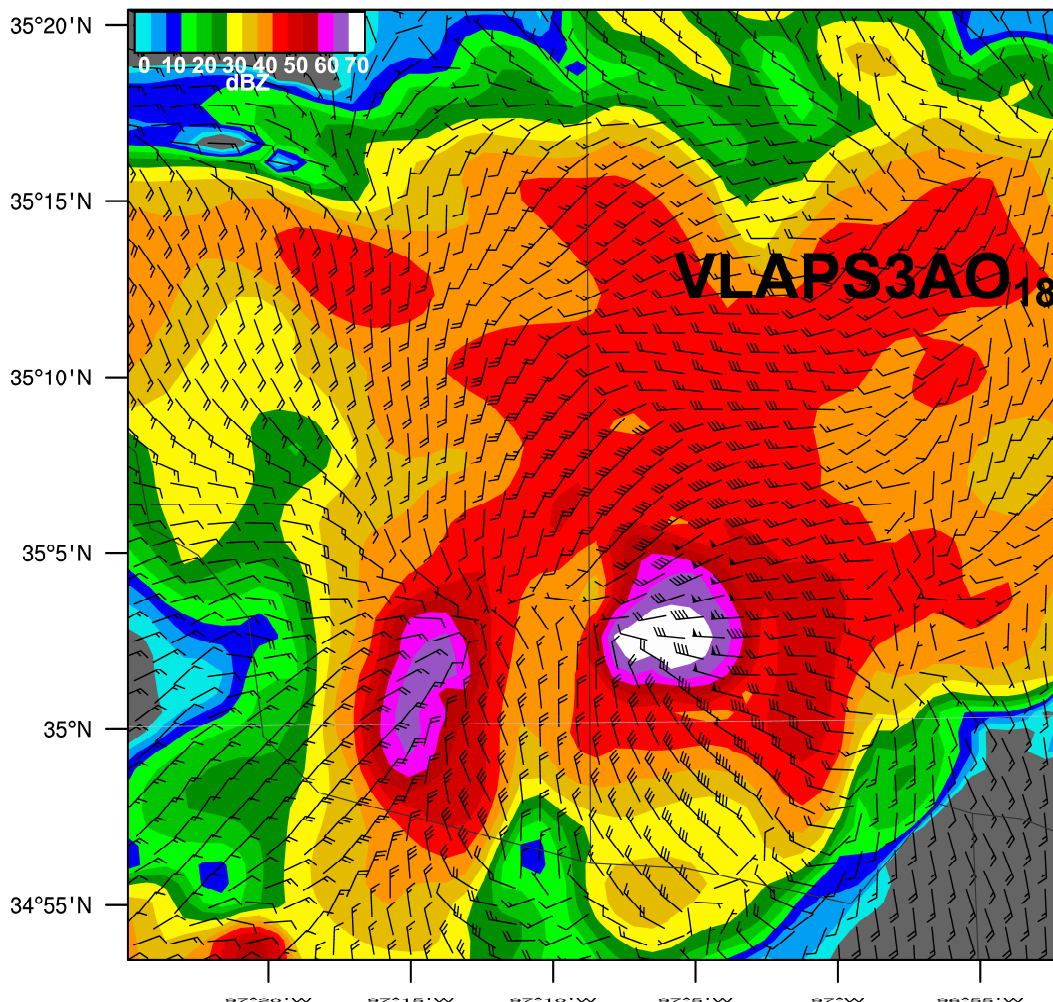


Fig. 19 WRF-ARW lowest model level radar reflectivity at 2015 UTC on 20 May 2013 for VLAPS3AO₁₈ zoomed into the area denoted by the white box in Fig. 18. Each half barb is 2.5 ms^{-1} and each full barb is 5.0 ms^{-1} .

A vertical cross section of the storm (Fig. 20) shows 2 narrow cores of high reflectivity ($\sim 70 \text{ dBZ}$) and some graupel. The stronger and farther eastern core has strong vertical motion just east of it; the area of graupel includes the area above this updraft. An anvil is also predicted stretching well east of the horizontal extent of the storm at ground level. It is difficult to see the full model structure of the main storm in this cross section since for clarity wind is plotted at many fewer grid points than are present in the model (horizontally wind vectors are plotted every ≈ 5 grid points).

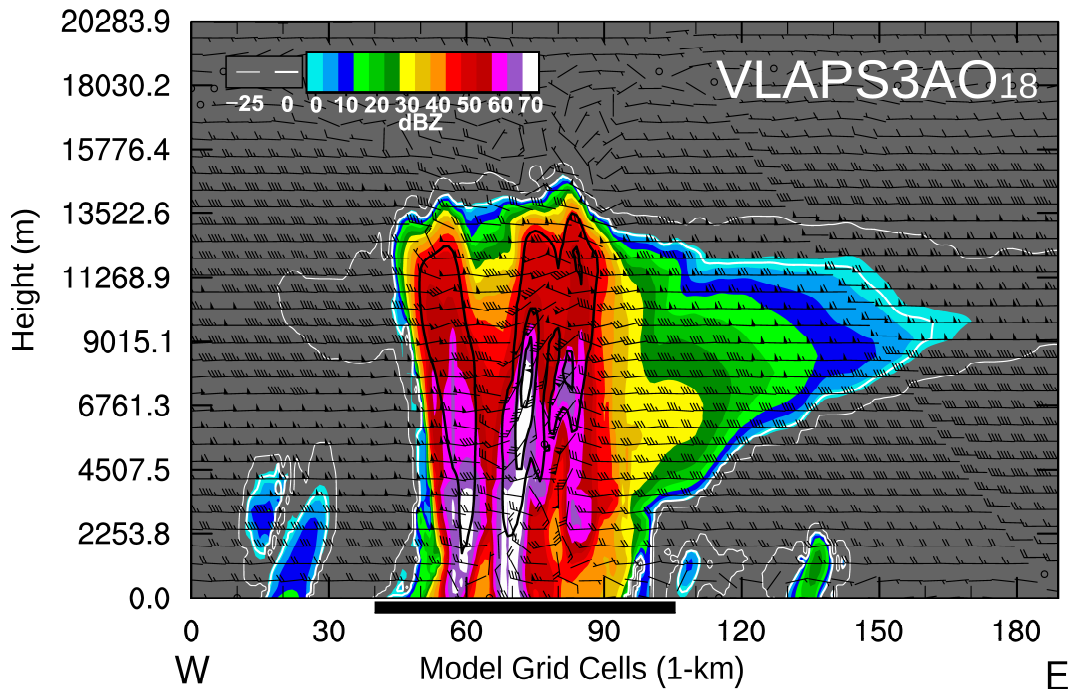


Fig. 20 Cross section of VLAPS3AO₁₈ along the white horizontal line in Fig. 18 showing winds in the plane (i.e., the model u- and w-component winds since this cross section is along the model x-dimension), model simulated radar reflectivity (shaded with a thick white line indicating the 0 dBZ isoline and a thin white line indicating the -25 dBZ isoline), and graupel mixing ratio (black contours every 3 g kg⁻¹). The thick black line at the bottom of the plot indicates the portion of the cross section included in Figs. 21 and 22. Each half barb is 2.5 ms⁻¹, each full barb is 5.0 ms⁻¹, and each flag is 25.0 ms⁻¹.

The model-predicted structure of this storm is seen more clearly in the zoomed-in cross section in Fig. 21. Near the surface, just east of the highest reflectivity values (i.e., approximately model grid cell 32 in terms of the x-axis label), the model predicts strong west winds (≈ 28 ms⁻¹), consistent with an outflow. About 10 km farther east (e.g., model grid cell 42), the flow in the transect just above the surface reverses from west to east, with the east wind serving as the inflow to a strong updraft between model grid cells 38–42. The updraft includes a region with weaker echoes than found to the west and to the east, but the magnitude of the echoes is still notable. By 7,000 m AGL in the updraft, the reflectivity increases to approximately 65 dBZ with an area of graupel and graupel mixing ratios exceeding 6 g kg⁻¹ around 8,000 m AGL. Just to the west of the column containing the strong updraft with graupel in its upper portion is a column with strong reflectivity reaching down to the surface. For grid cells 28–32, approximately 70 dBZ reflectivities reach the surface and 3g kg⁻¹ graupel mixing ratios reach as low as 2,250 m AGL (graupel mixing ratios of ≥ 9 g kg⁻¹ are forecasted around 7,000 m AGL near grid cell 32). Reflectivities greater than or equivalent to 60 dBZ cover most of the column between 0 and 7,000 m AGL for

grid cells 26–32. The main updraft in the storm is strong (Fig. 22), peaking at greater than 35 ms^{-1} around 6,700 m AGL around grid cell 41. There are also strong updrafts predicted at the top of the main column with high reflectivities; updrafts peak at greater than 35 ms^{-1} around 9,000 m AGL around grid cell 34.

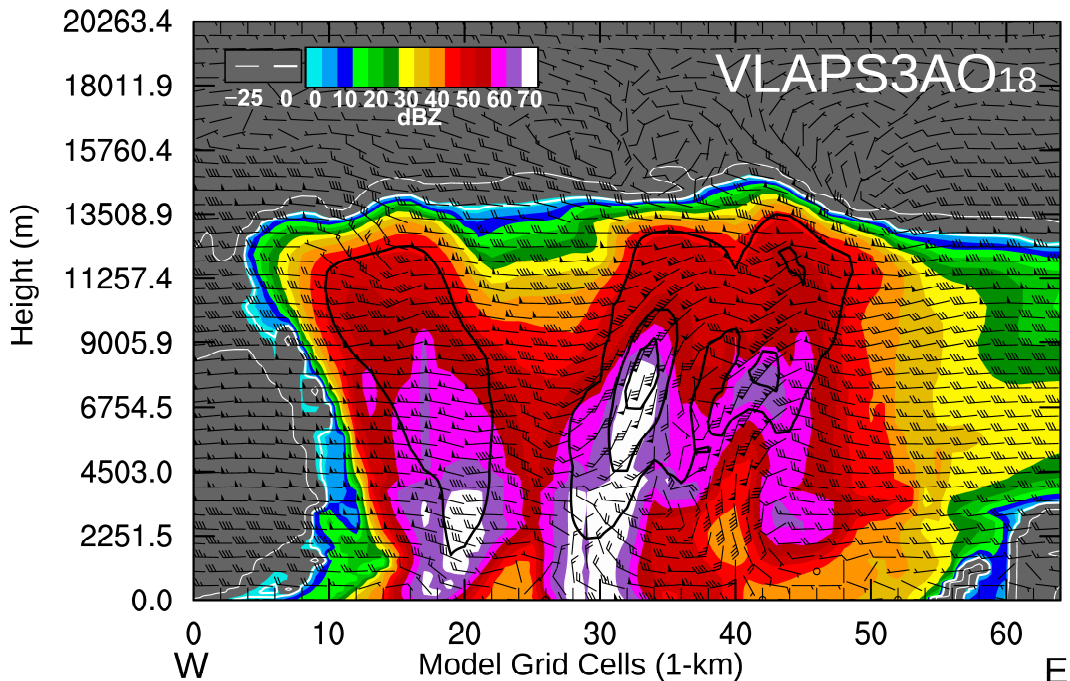


Fig. 21 Cross section of VLAPS3AO₁₈ along the portion of the cross section in Fig. 20 indicated by the thick black line along the bottom of that figure. This cross section shows winds in the plane (i.e., the model u- and w-component winds since this cross section is along the model x-dimension), model-simulated radar reflectivity (shaded with a thick white line indicating the 0 dBZ isoline and a thin white line indicating the -25 dBZ isoline), and graupel mixing ratio (black contours every 3 g kg^{-1}). Each half barb is 2.5 ms^{-1} , each full barb is 5.0 ms^{-1} , and each flag is 25.0 ms^{-1} .

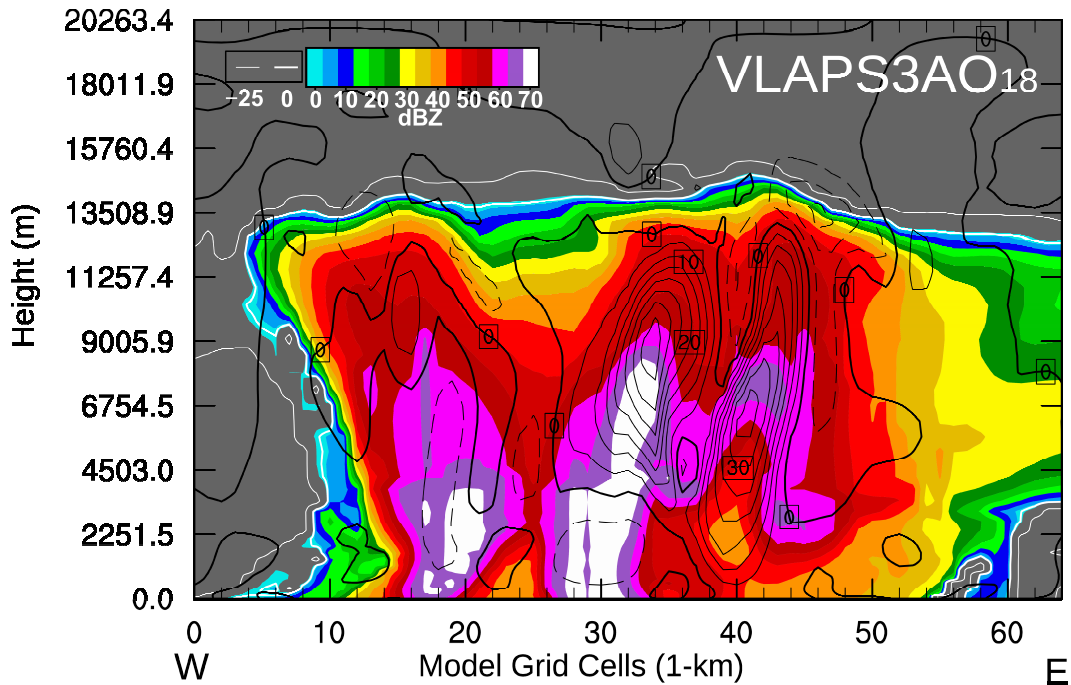


Fig. 22 Cross section of VLAPS3AO₁₈ along the portion of the cross section in Fig. 20 indicated by the thick black line along the bottom of that figure. This cross section shows model-simulated radar reflectivity (shaded with a thick white line indicating the 0 dBZ isoline and a thin white line indicating the -25 dBZ isoline), and vertical motion (black contours every 5 ms⁻¹ with contours representing downward motion dashed). Vertical motion ranges from -16 to +38 ms⁻¹ in this cross section.

VLAPS3AO₁₈ is able to forecast strong moist convection, with elements consistent with those expected to be present in strong convection. The reflectivities, horizontal wind speed, updrafts, and graupel predicted by the model are consistent elements expected in a strong thunderstorm. This example demonstrates the capability of this WRF configuration to simulate strong moist convection.

7. Summary, Discussion, and Conclusions

A preliminary analysis of WRF simulations using vLAPS analysis in combination with observation and analysis nudging data assimilation suggests potential value to this new combination data assimilation method when evaluated for a single case. The vLAPS nudging methodology combines 2 data assimilation techniques both with limited computational requirements. The methodology leverages the ability of vLAPS to create analyses containing in situ and remotely sensed data with the ability of nudging to assimilate continuously and gradually. While observation nudging can assimilate observations of fields that are prognostic fields within the model, it cannot directly assimilate observations of fields such as radar reflectivity that are not model prognostic variables; vLAPS can assimilate

fields whether or not they are model prognostic variables. Although vLAPS accounts for temporal variability among the observations, the resultant analyses are normally directly inserted as the model initial conditions; analysis nudging allows these analyses to gradually affect the model solution as well as allowing the assimilation of a series of vLAPS analyses in a single model integration. The gradual assimilation of a series of vLAPS analyses should allow the model initial conditions at the end of the assimilation to be more consistent with the model dynamics and physics and thus more likely to be retained by the model.

In this study, the model experiments differed in the source of the initial conditions, whether analysis nudging, observation nudging, or neither were applied, and the amount of model integration time before the time designated as the 0-h forecast (i.e., the length of the model spin-up). For the initial conditions, a single cycle of the 3-km HRRR was either used directly, or used as the first-guess field for either a vLAPS analysis (variational for some fields) or an analysis performed by Obsgrid (modified multiscan Cressman analysis). Experiments using analysis nudging nudged toward vLAPS analyses, where experiments using observation nudging nudged toward various MADIS observation types. Additionally, multiple cycles of each experiment were performed, with a 1-h cycle interval and each cycle having no influence on the subsequent cycle. Given the 9 experiments and the 6 cycles per experiment, there are a large number of model integrations to evaluate, even accounting for the model simulations that served as one cycle in one experiment and as another cycle in another experiment. The large amount of model output to evaluate requires an objective methodology, but here we performed a preliminary subjective analysis by focusing on comparing model-predicted reflectivity to observed reflectivity at 2015 UTC. The primary goal is to evaluate whether a hybrid data assimilation approach combining analysis nudging toward vLAPS analysis and observation nudging performs better than either vLAPS or nudging alone.

The full hybrid experiment (VLAPS3AO) showed promise in its radar reflectivity predictions as compared to other experiments. There were indications that providing a longer time period for the model to spin up can be beneficial. Overall, it was difficult to determine from this limited subjective comparison which experiments performed best. It should also be noted that by looking at a single output time, we did not consider the potential that experiments might be producing convection that appears to be a poor forecast at the time evaluated (here 2015 UTC) due to the model forecasting a convective element too early or too late. The general consistency among the experiments in the overall forecast for moist convection (e.g., the strong south–west to north–east line of convection), combined with the significant variations among the forecasts on the

details of the convection, appears consistent with the work of Zhang et al. (2015, 2016) examining predictability for this case. A more quantitative and thorough analysis of our WRF simulations is needed to determine the potential value of the different assimilation techniques, in light of the limits of predictability suggested by Zhang et al. (2015, 2016).

We also demonstrated the capability of VLAPS3AO to simulate strong moist convection. A storm predicted by VLAPS3AO was discussed that included various elements associated with strong moist convection. WRF predicted 70+ dBZ reflectivities, 35+ ms^{-1} updrafts, and 25+ ms^{-1} outflow winds at the surface, along with predicting graupel in the storm.

A more objective and complete analysis is required to better characterize the relative value of the different assimilation techniques being evaluated in this study. Evaluating all cycles of all experiments at all forecast times objectively will allow for more definite conclusions to be drawn. Even then, it must be remembered that this is a single case, and future work should choose those experiments showing the best potential and evaluate them for further cases, including cases lacking the strong convection that characterized this case. Also, the evaluation of reflectivity fields is particularly difficult, given the strong gradients in the field, especially in convective precipitation. Object-based methods can provide improved insight during the evaluation of radar-reflectivity forecasts but can be challenging and time consuming to apply well.

In addition to evaluating additional case days, other areas of future research would also be beneficial. The analysis nudging toward vLAPS analyses is currently limited to the fields WRF has the capability to nudge toward (potential temperature, water vapor mixing ratio, and winds). Future work could explore analysis nudging toward other fields in the vLAPS analyses (e.g., cloud water mixing ratio) to more fully utilize the vLAPS analyses. Other sources of analyses to nudge toward could also be explored.

This report describes the combination of nudging and vLAPS data assimilation techniques and provides preliminary results from the application of this technique to a single case day. The combination technique shows promise in that it can assimilate observations of both prognostic WRF fields (e.g., water vapor, potential temperature, and winds) and other fields (e.g., radar reflectivity) and can do so in a framework that gradually applies the effects of these observations to the model solution which, it is hoped, will allow the model to better retain the analyses than if they were inserted into the model at a single time step. Further analysis of this case is needed to better understand the value of the combination, and further case studies are needed to confirm results from the current study.

8. References

- Albers S, McGinley J, Birkenheuer. The local analysis and prediction system (LAPS): analyses of clouds, precipitation, and temperature. *Weather and Forecasting*. 1996;11:273–287.
- Alexander C, Smirnova T, Hu M, Weygandt S, Dowell D, Olson J, Benjamin S, James E, Brown J, Hofmann P, Lin H, Brundage K, and Jamison B. Recent advancements in convective-scale storm prediction with the coupled rapid refresh (RAP) / high-resolution rapid refresh (HRRR) forecast system. 14th Annual WRF Users' Workshop; 2013; Boulder, CO [accessed 2017 July 10]. <http://www2.mmm.ucar.edu/wrf/users/workshops/WS2013/ppts/2.3.pdf>.
- Atkins NT, Butler KM, Flynn KR, Wakimoto RM. An integrated damage, visual, and radar analysis of the 2013 Moore Oklahoma EF5 tornado. *Bulletin of the American Meteorological Society*. 2014;95:1549–1561.
- Benjamin SG, et al. 2A North American hourly assimilation and model forecast cycle: the rapid refresh. *Monthly Weather Review*. 2016;144:1669–1694.
- Brewster KA, Stratman DR. Tuning an analysis and incremental analysis updating assimilation for an efficient high-resolution forecast system. 20th Conference on Integrated Observing and Assimilation Systems for the Atmosphere, Oceans and Land Surface (IAOS-AOLS); 2016; New Orleans, LA [accessed 2017 July 10]. <https://ams.confex.com/ams/96Annual/webprogram/Paper289235.html>.
- Briggs WL. A Multigrid Tutorial. Society for Industrial and Applied Mathematics; 1987; Lancaster Press; 88 pp.
- Burgess D, Ortega K, Stumpf G, Garfield G, Karstens C, Meyer T, Smith B, Speheger D, Ladue J, Smith R, Marshall T. Moore, Oklahoma, tornado: damage survey and analysis. *Weather and Forecasting*. 2014;29:1229–1237.
- Chen F, Dudhia J. Coupling an advanced land surface–hydrology model with the Penn State–NCAR MM5 modeling system. Part I: model implementation and sensitivity. *Monthly Weather Review*. 2001;129:569–585.
- De Pondeca MSFV, et al. The real-time mesoscale analysis at NOAA's National Centers for Environmental Prediction: current status and development. *Weather and Forecasting*. 2011;26:593–612.
- Dowell DC, Wicker LJ, Snyder C. Ensemble Kalman filter assimilation of radar observations of the 8 May 2003 Oklahoma City supercell: influences of

- reflectivity observations on storm-scale analyses. *Monthly Weather Review*. 2011;139:272–294.
- Dudhia J. Numerical study of convection observed during the Winter Monsoon Experiment using a mesoscale two-dimensional model. *Journal of Atmospheric Sciences*. 1989;46:3077–3107.
- Expósito FJ, Gonzalez A, Perez JC, Diaz JP, Taima D. High-resolution future projections of temperature and precipitation in the Canary Islands. *Journal of Climate*. 2015;28:7846–7856.
- Gilliam RC, Godowitch JM, Rao ST. Improving the horizontal transport in the lower troposphere with four dimensional data assimilation. *Atmos Environ*. 2012;53:186–201.
- Hanley KE, Barrett AI, Lean HW. Simulating the 20 May 2013 Moore, Oklahoma tornado with a 100-metre grid-length NWP model. *Atmospheric Science Letters*. 2016;17:453–461.
- Hiemstra C, Liston G, Pielke R Sr, Birkenheuer D, Albers S. Comparing Local Analysis and Prediction System (LAPS) assimilations with independent observations. *Weather and Forecasting*. 2006;21:1024–1040.
- Hu M, Xue M, Brewster K. 3DVAR and cloud analysis with WSR-88D level-II data for the prediction of the Fort Worth, Texas, tornadic thunderstorms. Part I: cloud analysis and its impact. *Monthly Weather Review*. 2006;134:675–698.
- Janjić Z. Nonsingular implementation of the Mellor-Yamada level 2.5 scheme in the NCEP Meso model. College Park (MD): National Centers for Environmental Prediction; 2001. NCEP Office Note 437 [accessed 2017 July 10]. <http://www.lib.ncep.noaa.gov/ncepoofficenotes/files/on437.pdf>.
- Jiang H, Albers S, Xie Y, Toth Z, Jankov I, Scotten M, Picca J, Stumpf G, Kingfield D, Birkenheuer D, Motta B. Real-time applications of the variational version of the local analysis and prediction system (vLAPS). *Bulletin of the American Meteorological Society*. 2015;96:2045–2057.
- Kurdzo JM, Bodine DJ, Cheong BL, Palmer RD. High-temporal resolution polarimetric x-band 58oppler radar observations of the 20 May 2013 Moore, Oklahoma, tornado. *Monthly Weather Review*. 2015;143: 2711–2735.
- Lawless AS, Nichols NK, Ballard SP. A comparison of two methods for developing the linearization of a shallow-water model. *Quarterly Journal of the Royal Meteorological Society*. 2003;129:1237–1254.

- Lee JA, Kolczynski WC, McCandless TC, Haupt SE. An objective methodology for configuring and down-selecting an NWP ensemble for low-level wind prediction. *Monthly Weather Review*. 2012;140:2270–2286.
- Lei L, Hacker JP. Nudging, ensemble, and nudging ensembles for data assimilation in the presence of model error. *Monthly Weather Review*. 2012;143:2600–2610.
- Lei L, Stauffer DR, Haupt SE, Young GS. A hybrid nudging-ensemble Kalman filter approach to data assimilation. Part I: application in the Lorenz system. *Tellus A*. 2012a;64.
- Lei L, Stauffer DR, Deng A. A hybrid nudging-ensemble Kalman filter approach to data assimilation. Part II: application in a shallow-water model. *Tellus A*. 2012b;64.
- Lei L, Stauffer DR, Deng A. A hybrid nudging-ensemble Kalman filter approach to data assimilation in WRF/DART. *Quarterly Journal of the Royal Meteorological Society*. 2012c;138:2066–2078.
- Liu Y, Wu Y, Pan L, Bourgeois A, Roux G, Knierel JC, Hacker J, Pace J, Gallagher FW, Halvorson SF. Recent developments of NCAR's 4D-Relaxation Ensemble Kalman Filter system. 19th Conference on Integrated Observing and Assimilation Systems for the Atmosphere, Oceans, and Land Surface (IOAS-AOLS), American Meteorological Society; 2015 Jan 5–8, Phoenix, AZ.
- Liu C, Xiao Q, Wang B. An ensemble-based four-dimensional variational data assimilation scheme. Part I: technical formulation and preliminary test. *Monthly Weather Review*. 2008;136:3363–3373.
- Lopez P. Direct 4D-Var assimilation of NCEP Stage IV radar and gauge precipitation data at ECMWF. *Monthly Weather Review*. 2011;139:2098–2116.
- Lorenc AC, Rawlins F. Why does 4D-Var beat 3D-Var? *Quarterly Journal of the Royal Meteorological Society*. 2005;131:3247–3257.
- Mahfouf JF, Bauer P, Marecal V. The assimilation of SSM/I and TMI rainfall rates in the ECMWF 4D-Var system. *Quarterly Journal of the Royal Meteorological Society*. 2005;131:437–458.
- McGinley J, Albers S, Stamus P. Validation of a composite convective index as defined by a real-time local analysis system. *Weather and Forecasting*. 1991;6:337–356.

- Mlawer EJ, Taubman SJ, Brown PD, Iacono MJ, Clough SA. Radiative transfer for inhomogeneous atmospheres: RRTM, a validated correlated-k model for the longwave. *Journal of Geophysical Research: Atmospheres*. 1997;102:16663–16682.
- National Center for Atmospheric Research (NCAR). User's guide for the advanced Research WRF (ARW) modeling system version 3.8. Boulder (CO): National Center for Atmospheric Research; 2016 [accessed 2016 Aug 9]. http://www2.mmm.ucar.edu/wrf/users/docs/user_guide_V3.8/contents.html.
- National Centers for Environmental Information (NCEI). Storm events database. Silver Spring (MD): National Centers for Environmental Information; 2016 [accessed 2016 Aug 9]. <https://www.ncdc.noaa.gov/stormevents/>.
- Reen BP. Improving weather research and forecasting model initial conditions via surface pressure analysis. Army Research Laboratory (US): Adelphi Laboratory Center (MD); 2015 Sep. Report No.: ARL-TR-7447 [accessed 2017 July 10]. <http://www.arl.army.mil/arlreports/2015/ARL-TR-7447.pdf>.
- Reen BP. A brief guide to observation nudging in WRF. Boulder (CO): University Corporation for Atmospheric Research; 2016 [accessed 1 September 2016]. <http://www2.mmm.ucar.edu/wrf/users/docs/ObsNudgingGuide.pdf>.
- Reen BP, Dumais RE Jr, Passner JE. Mitigating excessive drying from the use of observations in mesoscale modeling. *Journal of Applied Meteorology and Climatology*. 2016;55:365–388.
- Reen BP, Schmehl KJ, Young GS, Lee JA, Haupt SE, Stauffer DR. Uncertainty in contaminant concentration fields resulting from atmospheric boundary layer depth uncertainty. *Journal of Applied Meteorology and Climatology*. 2014;53:2610–2626.
- Reen BP, Stauffer DR. Data assimilation strategies in the planetary boundary layer. *Boundary Layer Meteorol*. 2010;137:237–269.
- Rogers RE, Deng A, Stauffer DR, Gaudet BJ, Jia Y, Soong ST, Tanrikulu S. Application of the weather research and forecasting model for air quality modeling in the San Francisco Bay Area. *Journal of Applied Meteorology and Climatology*. 2013;52:1953–1973.
- Schroeder AJ, Stauffer DR, Seaman NL, Deng A, Gibbs AM, Hunter GK, Young GS. Evaluation of a high-resolution, rapidly relocatable meteorological nowcasting and prediction system. *Monthly Weather Review*. 2006;134:1237–1265.

- Shaw BL, Carpenter RL, Jr., Spencer PL, DuFran Z. Commercial implementation of WRF with efficient computing and advanced data assimilation. 9th Annual WRF User's Workshop; 2008; Boulder, CO [accessed 2017 July 17]. <http://www2.mmm.ucar.edu/wrf/users/workshops/WS2008/abstracts/2-05.pdf>.
- Skamarock WC, Klemp JB, Dudhia J, Gill DO, Barker DM, Duda M, Huang XY, Wang W, Powers JG. A description of the advanced research WRF version 3. Boulder (CO): National Center for Atmospheric Research; 2008. NCAR Tech Note 475 [accessed 2017 July 10]. http://www2.mmm.ucar.edu/wrf/users/docs/arw_v3.pdf.
- Snook N, Jung Y, Brotzge J, Putnam B, Xue M. Prediction and ensemble forecast verification of hail in the supercell storms of 20 May 2013. *Weather and Forecasting*. 2016;31:811–825.
- Snyder C, Zhang F. Assimilation of simulated Doppler radar observations with an ensemble Kalman filter. *Monthly Weather Review*. 2003;131:1663–1677.
- Stauffer DR, Seaman NL. Use of four-dimensional data assimilation in a limited-area mesoscale model. Part I: experiments with synoptic-scale data. *Monthly Weather Review*. 1990;118:1250–1277.
- Stauffer DR, Seaman NL. Multiscale four-dimensional data assimilation. *Journal of Applied Meteorology*. 1994;33:416–434.
- Stauffer DR, Seaman NL, Binkowski FS. Use of four-dimensional data assimilation in a limited-area mesoscale model. Part II: effects of data assimilation within the planetary boundary layer. *Monthly Weather Review*. 1991;119:734–754.
- Thompson G, Field PR, Rasmussen RM, Hall WD. Explicit forecasts of winter precipitation using an improved bulk microphysics scheme. Part II: implementation of a new snow parameterization. *Monthly Weather Review*. 2008;136:5095–5115.
- Vincent CL, Hahmann AN. The impact of grid and spectral nudging on the variance of the near-surface wind speed. *JAMC*. 2015;54:1021–1038.
- Xiao Q, Sun J. Multiple-radar data assimilation and short-range quantitative precipitation forecasting of a squall line observed during IHOP_2002. *Monthly Weather Review*. 2007;135:3381–3404.

- Xie Y, Koch S, McGinley J, Albers S, Bieringer PE, Wolfson M, Chan M. A space–time multiscale analysis system: a sequential variational analysis approach. *Monthly Weather Review*. 2011;139:1224–1240.
- Xie Y, Lu C, Browning GL. Impact of formulation of cost function and constraints on three-dimensional variational data assimilation. *Monthly Weather Review*. 2002;130:2433–2447.
- Xie YF, MacDonald AE. Selection of momentum variables for a three-dimensional variational analysis. *Pure Appl Geophys*. 2011. DOI 10.1007/s00024-011-0374-3.
- Zhang Y, Zhang F, Stensrud DJ, Meng Z. Practical predictability of the 20 May 2013 tornadic thunderstorm event in Oklahoma: sensitivity to synoptic timing and topographical influence. *Monthly Weather Review*. 2015;143:2973–2997.
- Zhang Y, Zhang F, Stensrud DJ, Meng Z. Intrinsic predictability of the 20 May 2013 tornadic thunderstorm event in Oklahoma at storm scales. *Monthly Weather Review*. 2016;144:1273–1298.
- Zhao, Q, Cook J, Xu Q, Harasti P. Improving short-term storm predictions by assimilating both radar radial-wind and reflectivity observations. *Weather and Forecasting*. 2008;23:373–391.

List of Symbols, Abbreviations, and Acronyms

1-D	1-dimensional
3-D	3-dimensional
4-D	4-dimensional
3DVAR	3-dimensional variational
4DVAR	4-dimensional variational
ABL	atmospheric boundary layer
ACARS	Aircraft Communications Addressing and Reporting System
AGL	above ground level
ARL	US Army Research Laboratory
ARPS	Advanced Regional Prediction System
EnKF	ensemble Kalman filter
FGAT	first guess at appropriate time
GRIB	Gridded Binary
GSI	Gridpoint Statistical Interpolation
HNEnKF	hybrid nudging-ensemble Kalman filter
HRRR	High Resolution Rapid Refresh
LAPS	Local Analysis and Prediction System
MADIS	Meteorological Assimilation Data Ingest System
MYJ	Mellor-Yamada-Janjić
NCAR	National Center for Atmospheric Research
NetCDF	network common data format
NWP	numerical weather prediction
TKE	turbulent kinetic energy
UTC	Coordinated Universal Time
vLAPS	variational Local Analysis and Prediction System
WPS	WRF Preprocessing System

WRF	Weather Research and Forecasting model
WRF-ARW	Advanced Research version of the Weather Research and Forecasting model
WSR-88D	Weather Surveillance Radar, 1988, Doppler

1 DEFENSE TECHNICAL
(PDF) INFORMATION CTR
DTIC OCA

2 DIR ARL
(PDF) RDRL CIO LL
IMAL HRA MAIL & RECORDS MGMT

1 GOVT PRINTG OFC
(PDF) A MALHOTRA

3 ARL
(PDF) RDRL CIE M
R DUMAIS
H CAI
B REEN

INTENTIONALLY LEFT BLANK.